Acetylene (C2H2) and hydrogen cyanide (HCN) from IASI satellite observations: global distributions, validation, and comparison with model

Valentin Duflot, Catherine Wespes, Lieven Clarisse, Daniel Hurtmans, Yasmine Ngadi, N. Jones, C. Paton-Walsh, Juliette Hadji-Lazaro, C. Vigouroux, M. de Mazière, et al.

Atmos. Chem. Phys., 15, 10509–10527, 2015
www.atmos-chem-phys.net/15/10509/2015/
doi:10.5194/acp-15-10509-2015

Atmospheric Chemistry and Physics
Open Access

Acetylene (C_2H_2) and hydrogen cyanide (HCN) from IASI satellite observations: global distributions, validation, and comparison with model

V. Duflot[1,2], C. Wespes[1], L. Clarisse[1], D. Hurtmans[1], Y. Ngadi[1], N. Jones[3], C. Paton-Walsh[3], J. Hadji-Lazaro[4], C. Vigouroux[5], M. De Mazière[5], J.-M. Metzger[6], E. Mahieu[7], C. Servais[7], F. Hase[8], M. Schneider[8], C. Clerbaux[1,4], and P.-F. Coheur[1]

[1]Spectroscopie de l'Atmosphère, Service de Chimie Quantique et Photophysique, Université Libre de Bruxelles (U.L.B.), 50 Av. F. D. Roosevelt, 1050, Brussels, Belgium
[2]Laboratoire de l'Atmosphère et des Cyclones (LACy), Université de la Réunion, UMR CNRS-Météo-France 8105, Saint-Denis de la Réunion, France
[3]School of Chemistry, University of Wollongong, Wollongong, New South Wales, Australia
[4]UPMC Université Paris 06, Université Versailles-St. Quentin, CNRS/INSU, LATMOS-IPSL, Paris, France
[5]Belgian Institute for Space Aeronomy (BIRA-IASB), 3, Av. Circulaire, 1180, Brussels, Belgium
[6]UMS3365 de l'OSU-Réunion, CNRS – Université de la Réunion, Saint Denis de la Réunion, France
[7]Institut d'Astrophysique et de Géophysique, Université de Liège, 17, Allée du 6 Août, B-4000, Liège, Belgium
[8]Institute for Meteorology and Climate Research (IMK-ASF), Karlsruhe Institute of Technology, Karlsruhe, Germany

Correspondence to: V. Duflot (valentin.duflot@univ-reunion.fr)

Received: 13 April 2015 – Published in Atmos. Chem. Phys. Discuss.: 21 May 2015
Revised: 23 August 2015 – Accepted: 4 September 2015 – Published: 24 September 2015

Abstract. We present global distributions of C_2H_2 and hydrogen cyanide (HCN) total columns derived from the Infrared Atmospheric Sounding Interferometer (IASI) for the years 2008–2010. These distributions are obtained with a fast method allowing to retrieve C_2H_2 abundance globally with a 5 % precision and HCN abundance in the tropical (subtropical) belt with a 10 % (25 %) precision. IASI data are compared for validation purposes with ground-based Fourier transform infrared (FTIR) spectrometer measurements at four selected stations. We show that there is an overall agreement between the ground-based and space measurements with correlation coefficients for daily mean measurements ranging from 0.28 to 0.81, depending on the site. Global C_2H_2 and subtropical HCN abundances retrieved from IASI spectra show the expected seasonality linked to variations in the anthropogenic emissions and seasonal biomass burning activity, as well as exceptional events, and are in good agreement with previous spaceborne studies. Total columns simulated by the Model for Ozone and Related Chemical Tracers, version 4 (MOZART-4) are compared to the ground-based FTIR measurements at the four selected stations. The model is able to capture the seasonality in the two species in most of the cases, with correlation coefficients for daily mean measurements ranging from 0.50 to 0.86, depending on the site. IASI measurements are also compared to the distributions from MOZART-4. Seasonal cycles observed from satellite data are reasonably well reproduced by the model with correlation coefficients ranging from −0.31 to 0.93 for C_2H_2 daily means, and from 0.09 to 0.86 for HCN daily means, depending on the considered region. However, the anthropogenic (biomass burning) emissions used in the model seem to be overestimated (underestimated), and a negative global mean bias of 1 % (16 %) of the model relative to the satellite observations was found for C_2H_2 (HCN).

Published by Copernicus Publications on behalf of the European Geosciences Union.

Table 1. Global HCN and C_2H_2 sources and sinks ($Tg\,yr^{-1}$).

	HCN	C_2H_2
Sources		
Biomass burning	0.1–3.18	1.6
Biofuels	0.21	3.3
Fossil fuel	0.02–0.04	1.7
Residential coal	0.2	
Biogenic	0.2	
Total	0.47–3.22	6.6
Sinks		
Ocean uptake	1.1–2.6	
Reaction with OH	0.3	~ 6.6
Photolysis	0.2×10^{-2}	
Reaction with $O(^1D)$	0.3×10^{-3}	
Total	1.4–2.9	~ 6.6

1 Introduction

Hydrogen cyanide (HCN) and acetylene (or ethyne; C_2H_2) are ubiquitous atmospheric trace gases with medium lifetime, which are frequently used as indicators of combustion sources and as tracers for atmospheric transport and chemistry. Typical abundances of C_2H_2 (HCN) range from 1 to 2 (2 to 5) $\times 10^{15}$ molec cm^{-2} for background levels, and from 8 to 20 (30 to 40) $\times 10^{15}$ molec cm^{-2} for biomass burning plume levels (Rinsland et al., 1999, 2001, 2002; Zander et al., 1991; Zhao et al., 2002; Clarisse et al., 2011a; Vigouroux et al., 2012; Duflot et al., 2013). Table 1 summarizes the main sources and sinks for HCN and C_2H_2. For HCN, biomass burning is the primary source, followed by biofuel and fossil fuel combustions, and its primary sink is thought to be ocean uptake (Li et al., 2000, 2003). For C_2H_2, biofuel combustion is considered to be the dominant source, followed by fossil fuel combustion and biomass burning (Xiao et al., 2007). Reaction with hydroxyl radical (OH) is the main sink for C_2H_2, which may also act as a precursor of secondary organic aerosols (Volkamer et al., 2009).

With a tropospheric lifetime of 2–4 weeks for C_2H_2 (Logan et al., 1981) and 5–6 months for HCN (Li et al., 2000; Singh et al., 2003), these two species are interesting tracers for studying atmospheric transport. The study of the ratio C_2H_2 / CO (carbon monoxide) can also help to estimate the age of emitted plumes (Xiao et al., 2007).

Long-term local measurements of HCN and C_2H_2 are sparse and mainly performed from ground-based Fourier transform infrared (FTIR) spectrometer at selected stations of the Network for the Detection of Atmospheric Composition Change (NDACC; http://www.ndacc.org) (Vigouroux et al., 2012, and references therein). Global distributions of HCN and C_2H_2 may thus help to reduce the uncertainties remaining with regard to the magnitude of their sources and sinks, as well as to their spatial distribution and seasonality in the atmosphere (Li et al., 2009; Parker et al., 2011).

Satellite sounders have provided considerable new information in the past years, with measurements from the Atmospheric Chemistry Experiment (ACE-FTIR) (Lupu et al., 2009; González Abad et al., 2011), the Michelson Interferometer for Passive Atmospheric Sounding (MIPAS) (Parker et al., 2011; Wiegele et al., 2012; Glatthor et al., 2015) and the microwave limb sounder (MLS) (Pumphrey et al., 2011). These measurements were all made in limb geometry and consequently mostly in the upper troposphere or higher; also the spatial sampling from these instruments is limited, making it less well-suited when studying dynamical events on short timescales.

Having a twice daily global coverage and a 12 km diameter footprint at nadir, the Infrared Atmospheric Sounding Interferometer (IASI) infrared sounder (Clerbaux et al., 2009) aboard the MetOp-A satellite has the potential for providing measurements for these two species globally, and with higher spatial resolution and temporal sampling than what has been obtained up to now.

Previous studies have demonstrated that HCN and C_2H_2 can be observed with the IASI infrared nadir-looking hyperspectral sounder, e.g. in a specific biomass burning plume (Clarisse et al., 2011a), as well as in an anthropogenic pollution plume uplifted in the free troposphere (Clarisse et al., 2011b). More recently, Duflot et al. (2013) have shown that HCN and C_2H_2 columns can be routinely retrieved from IASI spectra, even in the absence of exceptional columns or uplift mechanisms, when CO_2 line mixing is accounted for in the inversion scheme. These previous works were based on an optimal estimation method (OEM) developed and formalized by Rodgers (2000).

In this paper, we first present a fast scheme for the global detection and quantification of HCN and C_2H_2 total columns from IASI spectra. We describe 2008–2010 time series and analyze the seasonality of the columns of these two species above four NDACC sites in comparison with ground-based FTIR measurements. We finally present the global distributions for the years 2008 to 2010 that we compare with model outputs for these two species.

2 Instrument and method

2.1 IASI

IASI is on board the MetOp-A platform launched in a Sun-synchronous orbit around the Earth at the end of 2006. The overpass times are 09:30 and 21:30 MLT (mean local time). Combining the satellite track with a swath of 2200 km, IASI provides global coverage of the Earth twice a day with a footprint of 12 km at nadir. IASI is a Fourier transform spectrometer that measures the thermal infrared radi-

ation emitted by the Earth's surface and atmosphere in the 645–2760 cm^{-1} spectral range with a spectral resolution of 0.5 cm^{-1} apodized and a radiometric noise below 0.2 K between 645 and 950 cm^{-1} at 280 K (Clerbaux et al., 2009). The IASI spectra used in this study are calibrated radiance spectra provided by EUMETCast near-real-time service.

2.2 Retrieval strategy

Up to now, 24 trace gases have been detected from IASI radiance spectra, including HCN and C_2H_2 (see Clarisse et al., 2011a, for the list of detected species), with an OEM (Rodgers, 2000) implemented in a line by line radiative transfer model called Atmosphit (Coheur et al., 2005). In the cases of HCN and C_2H_2, the accuracy of the retrievals has been recently improved by taking into consideration the CO_2 line mixing in the radiative transfer model (Duflot et al., 2013). This retrieval method, relying on spectral fitting, needs a high computational power and is time-consuming, especially when a large number of spectra has to be analyzed and fitted. This is therefore not suitable for providing global-scale concentration distributions of these trace gases in a reasonable time.

One of the commonly used methods for the fast detection of trace gases is the brightness temperature difference (BTD) between a small number of channels, some being sensitive to the target species, some being not. Such a method has been used from IASI spectra for sulfur dioxide (SO_2) (Clarisse et al., 2008) and ammonia (NH_3) (Clarisse et al., 2009). It is of particular interest in operational applications (quick alerts) or when large amounts of data need to be processed. However, relying on a cautious selection of channels to avoid the contamination with other trace gases, the BTD method does not fully exploit all the information contained in hyperspectral measurements. Especially, low concentrations of the target species may not be detected with such a method.

Walker et al. (2011) presented a fast and reliable method for the detection of atmospheric trace gases that fully exploits the spectral range and spectral resolution of hyperspectral instruments in a single retrieval step. They used it to retrieve SO_2 total column from a volcanic plume and NH_3 total column above India. More recently, Van Damme et al. (2014) presented a retrieval scheme to retrieve NH_3 from IASI spectra based on the work of Walker et al. (2011), and introduced a metric called hyperspectral range index (HRI). We use in the present study a similar approach.

2.2.1 Hyperspectral range index

The method used in this study is a non-iterative pseudo retrieval method of a single physical variable or target species x expressed following the formalism developed by Rodgers (2000):

$$\hat{x} = x_0 + (K^T S_\epsilon^{\mathrm{tot}-1} K)^{-1} K^T S_\epsilon^{\mathrm{tot}-1} (y - F(x_0)), \quad (1)$$

where y is the spectral measurements, x_0 is the linearization point, F is the forward model (FM), $S_\epsilon^{\mathrm{tot}}$ is the covariance of the total error (random + systematic), and the Jacobian K is the derivative of the FM to the target species in a fixed atmosphere.

$S_\epsilon^{\mathrm{tot}}$ can be estimated considering an appropriate ensemble of N measured spectra, which can be used to build up the total measurement error covariance S_y^{obs}:

$$S_\epsilon^{\mathrm{tot}} \simeq \frac{1}{N-1} \sum_{j=1}^{N} (y_j - \bar{y})(y_j - \bar{y})^T = S_y^{\mathrm{obs}}, \quad (2)$$

where $\bar{y}$ is the calculated mean spectrum for the ensemble.

To generate S_y^{obs}, we randomly chose one million cloud free spectra observed by IASI all over the world, above both land and sea, during the year 2009. Then, we applied a BTD test to remove the spectra contaminated by the target species. For HCN (C_2H_2), the wave numbers 716.5 and 732 cm^{-1} (712.25 and 737.75 cm^{-1}) were used as reference channels and 712.5 cm^{-1} (730 cm^{-1}) was used as test channel (Fig. 1, middle panel). Given the medium lifetimes of the target species (few weeks for C_2H_2 to few months for HCN), and the limited accuracy of the BTD test due to the weak spectral signatures of the target species, it is likely that such randomly chosen and filtered spectra still contain a small amount of the target species whose signal may come out from the noise. This limitation decreases the sensitivity of the method, which is discussed in Sect. 2.2.3.

The spectral ranges considered to compute the S_y^{obs} matrices are 645–800 cm^{-1} for HCN and 645–845 cm^{-1} for C_2H_2 (Fig. 1, top panel). These ranges were chosen as they include parts of the spectrum which have a relatively strong signal from the target species but also from the main interfering species (CO_2, H_2O and O_3; Fig. 1, bottom panel) in order to maximize the contrast with the spectral background.

Having calculated S_y^{obs} and , the HRI of a measured spectrum y can be defined as

$$\mathrm{HRI} = G(y - \bar{y}) \quad (3)$$

with G the measurement contribution function

$$G = (K^T S_y^{\mathrm{obs}-1} K)^{-1} K^T S_y^{\mathrm{obs}-1} \quad (4)$$

The HRI is a dimensionless scalar similar, other than units, to the apparent column retrieved in Walker et al. (2011). Unlike the optimal estimation method, no information about the vertical sensitivity can be extracted. Note also that the use of a fixed Jacobian to calculate HRI does not allow for generating meaningful averaging kernels.

2.2.2 Conversion of HRI into total columns

Having calculated the matrices G for HCN and C_2H_2, each observed spectrum can be associated through Eq. (3) with

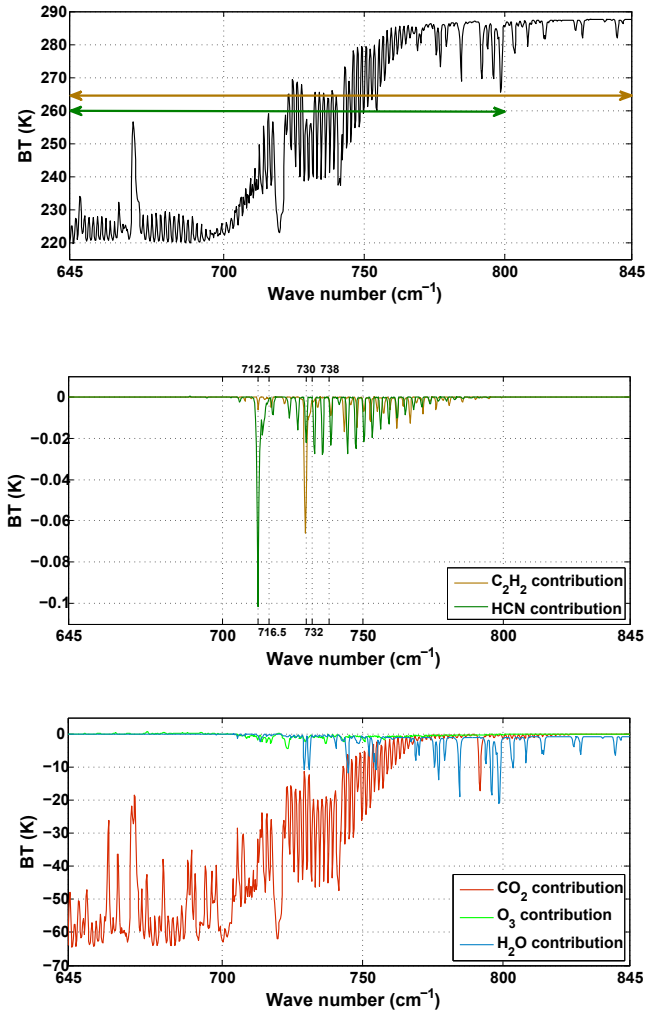

Figure 1. (Top) Simulated spectra in the region of the HCN ν_2 band and C_2H_2 ν_5 band. The green (brown) double sided arrow gives the spectral range used to compute the S_ϵ matrices for HCN (C_2H_2). (Middle) contributions of climatological background levels of HCN and C_2H_2. (Bottom) contribution of CO_2 (red line), O_3 (green line) and H_2O (blue line) to a simulated spectrum for background concentrations. Calculations have been made for the US standard atmosphere (Standard Atmosphere: National Atmospheric and Oceanic Administration, 1976) with CO_2 concentrations scaled to 390 ppmv.

a value of HRI for HCN (HRI_{HCN}) and C_2H_2 ($HRI_{C_2H_2}$). These HRIs are only metrics for determining whether levels of the gas are enhanced with respect to the climatological background over the vertical levels where the instrument is sensitive. For a given atmosphere (atm), the main challenge is then to link the HRI to a column amount of the target molecule, i.e. to find $B_{HCN_{atm}}$ and $B_{C_2H_{2atm}}$ (in molec cm^{-2}) such as

$$[X] = B_{X_{atm}} HRI_X, \quad (5)$$

$[X]$ being the species abundance in molec cm^{-2}.

To determine these coefficients linking the HRIs to total column amounts, HCN and C_2H_2 profiles have been constructed, with enhanced concentrations of the species located in a 1 km thick layer, whose altitude is varied from the ground up to 30 km for HCN and up to 20 km for C_2H_2 (the choice of these maximum altitudes are made with respect to the Jacobians of the FM that are shown in Fig. 3 and commented on in Sect. 2.2.3). Each of the constructed profile has been associated with a spectrum through the FM of Atmosphit considering standard absorption profiles from modelled atmospheres for the other species. The associated values of HRI_{HCN} and $HRI_{C_2H_2}$ have then been computed for each of the simulated spectra. Figure 2 shows the look up tables (LUTs) of HRI_{HCN} (top) and $HRI_{C_2H_2}$ (bottom) as a function of the abundance of the target molecule and of the altitude of the polluted layer in a standard tropical modelled atmosphere (Anderson et al., 1986). Similar LUTs have been computed for standard temperate (US standard atmosphere) and polar (Anderson et al., 1986) atmospheres (data not shown). The satellite viewing angles were taken into account in the HRI calculation similarly to Van Damme et al. (2014). One can see that, for a given atmosphere and for a given altitude of the polluted layer, the abundances of both species linearly depend on the HRI value, which validates Eq. (5). For a given atm and a given species X, the different values of B with respect to the altitude z of the polluted layer will be noted $b_{X_{atm}}(z)$ and $b_{X_{atm}}(z)$ (in molec cm^{-2}) in the following.

Figure 3 shows the normalized Jacobians of the FM for HCN and C_2H_2 averaged over the spectral ranges given in Sect. 2.2.1 (645–800 cm^{-1} for HCN and 645–845 cm^{-1} for C_2H_2) and for each of the three standard modelled atmospheres. These Jacobians express the sensitivity of the FM, i.e. both the radiative transfer model and IASI (through its instrumental function), to the target species abundance X in a fixed atm:

$$K_{X_{atm}} = \left[\frac{\partial F_{atm}}{\partial X}(z_1)\ldots\frac{\partial F_{atm}}{\partial X}(z_n)\right] = [k_{X_{atm}}(z_1)\ldots k_{X_{atm}}(z_n)]. \quad (6)$$

We then obtain the coefficients $B_{X_{atm}}$ by multiplying the $b_{X_{atm}}(z)$ by the value of the Jacobian at the altitude z:

$$B_{X_{atm}} = \sum_{i=1}^{n}\left(b_{X_{atm}}(z_i) \times k_{X_{atm}}(z_i)\right) \quad \text{with} \sum_{i=1}^{n} k_{X_{atm}}(z_i) = 1. \quad (7)$$

Applying this method to the three standard modelled atmospheres (tropical, temperate and polar), we get a B_X value for each, which we have associated with the corresponding range of latitude ([±20°], [±45° : ±60°], [±75° : ±90°], respectively), and linearly interpolated between. Figure 4 gives the resulting values of B_{HCN} (blue) and $B_{C_2H_2}$ (green) in a function of the latitude.

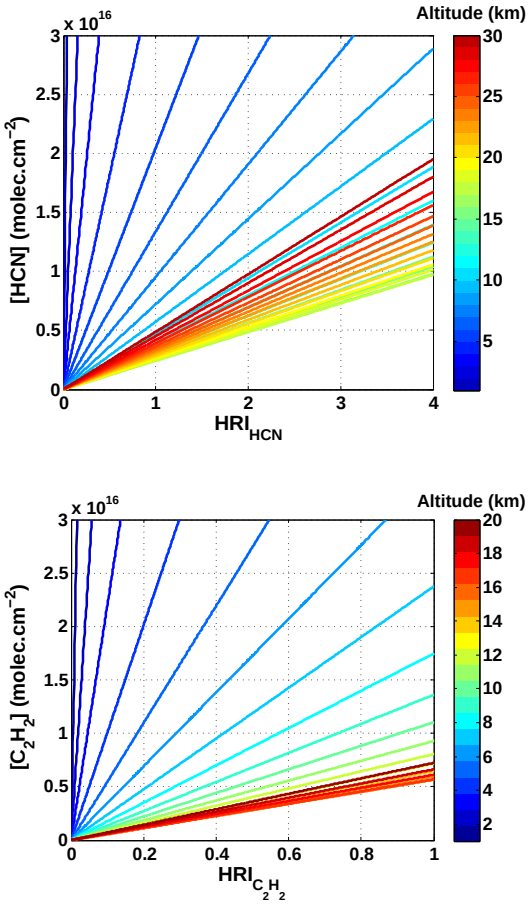

Figure 2. Variations of the HRI with HCN (top) and C_2H_2 (bottom) column (molec cm^{-2}) integrated over the 1 km thick polluted layer in a standard modelled subtropical atmosphere from forward model simulations. The colour scale gives the altitude of the polluted layer.

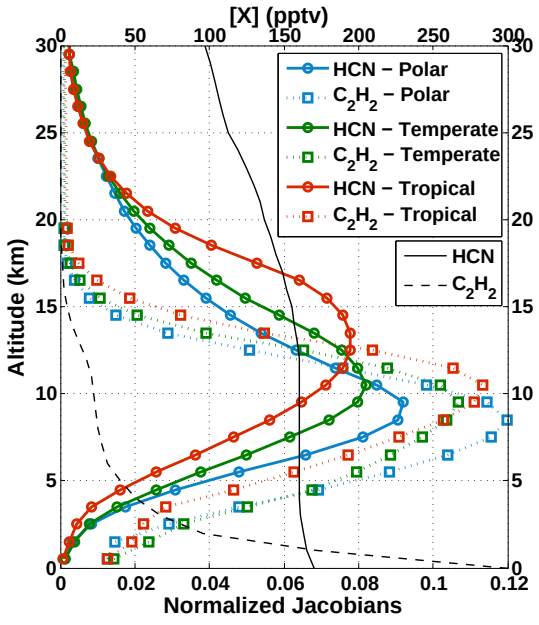

Figure 3. Normalized Jacobians of the forward model implemented in Atmosphit for HCN (solid lines) and C_2H_2 (dotted lines) and for the standard modelled polar (blue lines), temperate (green lines) and subtropical (red lines) atmospheres. These are averaged Jacobians over the spectral ranges 645–800 cm^{-1} for HCN and 645–845 cm^{-1} for C_2H_2. Are also plotted the HCN (black line) and C_2H_2 (black dashed line) vertical distributions in a standard temperate atmosphere.

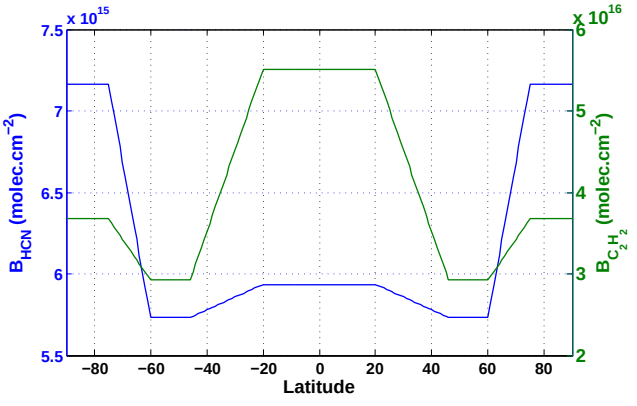

Figure 4. Values of B_{HCN} (blue) and $B_{C_2H_2}$ (green) as a function of the latitude.

2.2.3 Sensitivity and stability of the method

The sensitivity of the method can be assessed from the Jacobians presented in Fig. 3. For HCN, one can see that there is no sensitivity at the surface and above ∼ 30 km, and the altitude of the sensitivity peak is located close to the tropopause at ∼ 9 km, ∼ 11 km and ∼ 14 km for the polar, temperate and tropical atmospheres, respectively. For C_2H_2, there is no sensitivity above ∼ 20 km, and the maximum sensitivity is reached at ∼ 8, ∼ 10 and ∼ 11 km for the polar, temperate and tropical atmospheres, respectively. The vertical distribution in a standard temperate atmosphere (US standard atmosphere) is also shown for both species in Fig. 3. These standard distributions agree reasonably well (in shape and value) with observed profiles exhibited in previous studies (e.g. Li et al., 2003; Xiao et al., 2007). The C_2H_2 Jacobians match quiet well with the standard distribution of the molecule (i.e. from the ground up to ∼ 20 km), with somehow a lack of sensitivity close to the ground where C_2H_2 is the most abundant. For HCN, which shows a nearly "flat" vertical distribution up to 30 km, the Jacobians show a lack of sensitivity close to the ground and above 30 km, where HCN is still present (HCN distribution decreases down to 60 pptv at 60 km – data not shown).

The HRIs presented here above are sensitive to the abundance of the target species – this is what they are made for – and to their vertical distribution. However, once cloudy spectra have been discarded, the measured column amount may also depend on (1) the proper suppression of the spectral

background, (2) the conditions of thermal contrast (TC) with the surface, and (3) the accuracy of the FM to simulate the spectra used to build up the LUTs. The latter was discussed already by Duflot et al. (2013). In order to test the impact of the two first factors (spectral background suppression and TC) on the retrieved column amount, HCN and C_2H_2 profiles have been constructed with varying TC and concentrations of the interfering and target species. In general thermal contrast can be defined as the temperature difference between the surface and the air temperature at some altitude of interest. We consider here the same definition for the TC as in Van Damme et al. (2014): the TC is defined here as the difference between the skin (surface) temperature and that of the air at an altitude of 1.5 km. These variations in interfering species abundances and TC were considered to be independent and were taken within the range ±2 % for CO_2 and ±20 % for H_2O and O_3, and in the range ±10 K for the TC. For a fixed column amount of the target species, the HRIs were compared one by one to a HRI corresponding to a standard spectrum (i.e. with background concentrations of the interfering species and a TC equal to zero) and if the difference between the two HRIs was lower than 10 %, then this fixed abundance of the target species was tagged as independently detectable from the listed parameters.

The TC was found to be the major source of HRI variation for both target species, and a serious cause of limitation only for HCN. Figure 5 shows the variation of HRI_{HCN} caused by a TC equal to ±10 K. One can see that the HCN column amount can be detected with a variation due to the TC below 10 % when its abundance is higher than 0.28, 1.2 and 1.6×10^{16} molec cm^{-2} for the tropical, temperate and polar atmospheres, respectively. This gives the stability thresholds above which HCN column amount can be measured with a 10 % confidence in the independence of the retrieval method to the atmospheric parameters. Consequently, as the stability thresholds of the method for HCN in temperate and polar atmospheres are too high (1.2 and 1.6×10^{16} molec cm^{-2}, respectively) to allow for the detection of HCN background abundances as compared to usual background column of typically 0.35×10^{16} molec cm^{-2} (Vigouroux et al., 2012; Duflot et al., 2013), IASI HCN measurements have to be rejected in these two types of atmosphere, and considered in the tropical belt for values above 0.28×10^{16} molec cm^{-2}. In order to broaden the exploitable latitude range, we performed the same study for subtropical latitudes (considering a mix of tropical and temperate atmospheres), and we found a 25 % confidence in the independence of the retrieval method to the atmospheric parameters (data not shown). As a result, in the following, IASI HCN measurements are considered in the ±35° latitude band with a stability threshold of 0.28×10^{16} molec cm^{-2}, and confidence in the stability of the method is 10 % at tropical latitudes ([±20°]) and 25 % at subtropical latitudes ([±35° : ±20°]). Oppositely to HCN, for C_2H_2, the variation of $HRI_{C_2H_2}$ due to varying TC was found to be lower than 5 % for every C_2H_2 abundance (data not shown). Consequently, in the following no IASI C_2H_2 measurements are rejected.

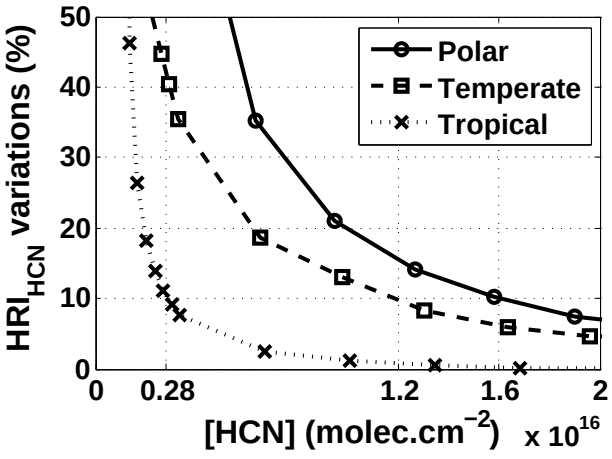

Figure 5. Variation of HRI_{HCN} caused by a TC equal to ±10 K for the polar (solid line an circles), temperate (dashed line and squares) and tropical (dotted line and crosses) atmospheres.

3 Results

The goal of this section is to describe and evaluate the C_2H_2 and HCN total columns as measured by IASI. We first compare HCN and C_2H_2 total columns retrieved from IASI spectra and from ground-based FTIR spectra. We then depict the C_2H_2 and HCN total columns at global and regional scales. IASI global and regional distributions are finally compared with output from the Model for Ozone and Related Chemical Tracers, version 4 (MOZART-4) in order to evaluate the agreement between the model and the IASI distributions.

3.1 Comparison with ground-based observations

We compare in this section HCN and C_2H_2 total columns retrieved from IASI spectra and from ground-based FTIR spectra for the years 2008–2010 for four selected ground-based FTIR observation sites (i.e. wherever observations for these two species were available during the period of study): Wollongong (34° S; 151° E; 30 m above mean sea level, a.m.s.l.), Reunion Island (21° S; 55° E; 50 m a.m.s.l.), Izaña (28°N; 16°W; 2367 m a.m.s.l.) and Jungfraujoch (46° N; 8° E; 3580 m a.m.s.l.) (Fig. 6). IASI cloudy spectra were removed from the data set using a 10 % contamination threshold on the cloud fraction in the pixel. As exposed in Sect. 2.2.3, errors in retrieved species abundances from IASI spectra due to variations in atmospheric parameters are 10 % at tropical latitudes ([±20°]) and 25 % at subtropical latitudes ([±35° : ±20°]) for HCN and 5 % for C_2H_2, and comparison with ground-based HCN measurements are only performed for tropical and subtropical sites (Reunion Island, Wollongong and Izaña).

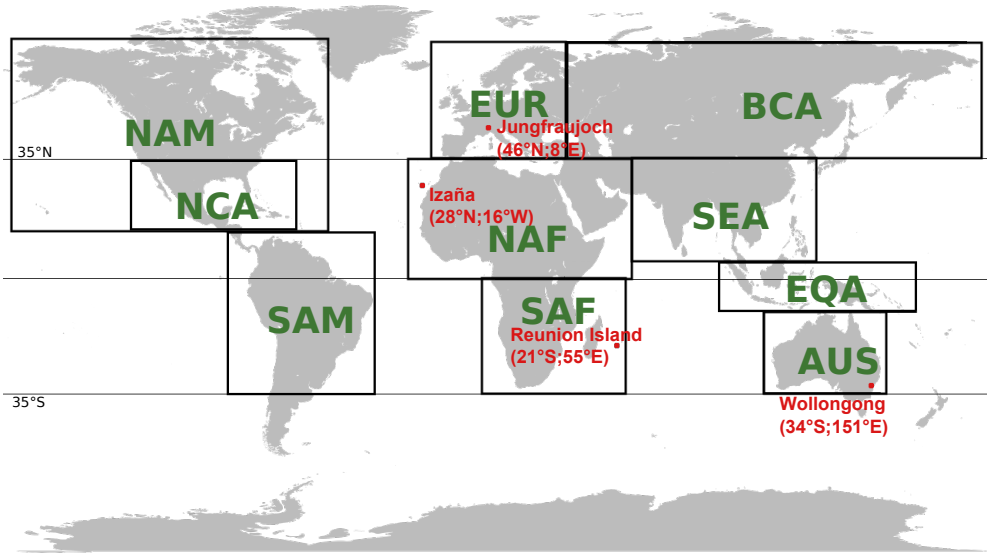

Figure 6. Locations of the four ground-based FTIR measurements sites (Jungfraujoch, Izaña, Reunion Island and Wollongong) and map of the 10 regions used in this study: NAM: northern America, NCA: north-central America, SAM: South America, EUR: Europe, NAF: northern Africa, SAF: southern Africa, BCA: boreal Central Asia, SEA: Southeast Asia, EQA: equatorial Asia, AUS: Australia.

The total error for ground-based measurements at Reunion Island is 17 % for both species, total error for HCN ground-based measurements at Wollongong is 15 %, total error for HCN ground-based measurements at Izaña is 10 %, and total error for C_2H_2 ground-based measurements at Jungfraujoch is 7 %. Detailed description of ground-based FTIR data set, retrieval method and error budget can be found in Vigouroux et al. (2012) for Reunion Island and in Mahieu et al. (2008) for Jungfraujoch. However, at Reunion Island, the retrieval strategies have been slightly improved from Vigouroux et al. (2012), mainly concerning the treatment of the interfering species, but the same spectral signatures are used. Izaña data set and error budget were obtained from the NDACC database (ftp://ftp.cpc.ncep.noaa.gov/ndacc/station/izana/). The Wollongong data set and error budget were calculated by N. Jones from the University of Wollongong, personal communication, 2014.

Figure 7 shows the mean total column averaging kernels for the ground-based FTIR at each of the four sites. Similar to IASI (Fig. 3), information content from ground-based instruments measurements is mostly in the middle-high troposphere for both species. The main difference can be observed for tropical C_2H_2: while IASI Jacobian peaks at 10 km for C_2H_2 in a tropical atmosphere, ground-based FTIR averaging kernel peaks at 15 km for C_2H_2 at Reunion Island.

Figure 8 shows the comparison between the IASI and the ground-based measurements. IASI retrieved total columns were averaged on a daily basis and on a $1° \times 1°$area around the observation sites. HCN retrieved abundances below 2.8×10^{15} molec cm^{-2} have been removed from both ground-based and space measurements to allow for comparison of both data sets (cf. Sect. 2.2.3). One can see that there is

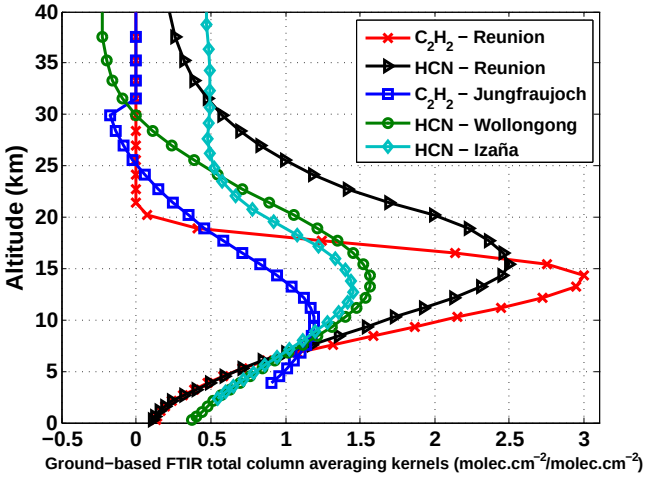

Figure 7. Total column averaging kernels of ground-based FTIR in molec cm^{-2}/molec cm^{-2} for C_2H_2 at Reunion Island (red stars and line), HCN at Reunion Island (black circles and line), HCN at Wollongong (green dots and line), HCN at Izaña (light blue diamonds and line) and C_2H_2 at Jungfraujoch (blue squares and line).

an overall agreement between the IASI and the ground-based FTIR measurements considering the error bars. An important result from this study is that IASI seems to capture the seasonality in the two species in most of the cases. This is best seen by looking at the IASI monthly mean retrieved total columns (black circles and lines in Fig. 8). The scatter of the IASI daily mean measurements (red dots) are due to the averaging on a $1° \times 1°$ area around the observation sites.

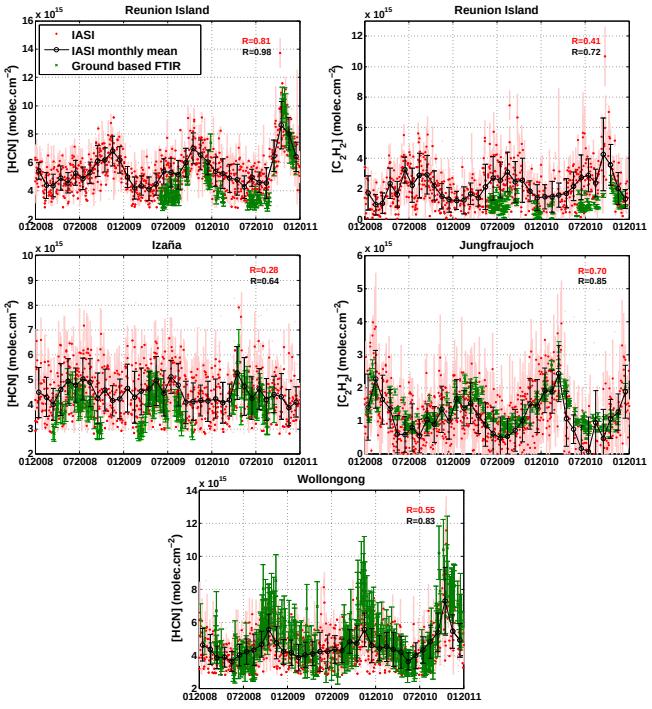

Figure 8. Time series of HCN (left panel) and C_2H_2 (right panel) measurements for Reunion Island (HCN and C_2H_2), Wollongong (HCN only), Izaña (HCN only), and Jungfraujoch (C_2H_2 only). IASI measurements are shown as daily and $1° \times 1°$ means (red dots) with associated standard deviations (light red lines), and as monthly and $1° \times 1°$ means (black circles and line) with associated standard deviation (vertical black lines). Ground-based FTIR measurements are shown as daily means with associated total error by green crosses and lines. Correlation coefficients are given on each plot for daily means in red and for monthly means in black.

At Reunion Island HCN and C_2H_2 peak in October–November and are related to the Southern Hemisphere biomass burning season (Vigouroux et al., 2012). IASI (ground-based FTIR) observed maxima are around 12 (10) $\times 10^{15}$ molec cm^{-2} for HCN and 10 (3) $\times 10^{15}$ molec cm^{-2} for C_2H_2. The seasonality and interannual variability matches very well with that of the ground-based FTIR measurements for HCN (correlation coefficient of 0.81 for the entire daily mean data set, and of 0.98 for the monthly mean data set) but with the IASI columns being biased high by 0.79×10^{15} molec cm^{-2} (17 %). For C_2H_2 at Reunion Island, the seasonality and interannual variability matches reasonably well that of the ground-based measurements (correlation coefficient of 0.40 for the entire daily mean data set, and of 0.72 for the monthly mean data set) but with the IASI columns being biased high by 1.10×10^{15} molec cm^{-2} (107 %). Such a high bias between the two data sets could be due to the difference between space and ground-based instruments sensitivity (Figs. 3 and 7). One can also notice that the C_2H_2 and HCN peaks are higher in 2010. As South American biomass burning plumes are known to impact trace gases abundance above Reunion Island (Edwards et al., 2006a, b; Duflot et al., 2010), these 2010 higher peaks are probably influenced by the 2010 great Amazonian fires (Lewis et al., 2011).

At Wollongong HCN peaks also in October–November due to the Southern Hemisphere biomass burning season (Paton-Walsh et al., 2010). We find maxima of around 11×10^{15} molec cm^{-2} in October 2010 for both space and ground-based instruments, which is, similar to Reunion Island, very likely to be a signature of the great Amazonian fires as South American biomass burning plumes are known to impact trace gases abundance above Australia (Edwards et al., 2006a, b). The seasonality and interannual variability matches well with that of the ground-based FTIR measurements (correlation coefficient of 0.55 for the entire daily mean data set, and of 0.83 for the monthly mean data set), with the IASI columns being biased low by 0.48×10^{15} molec cm^{-2} (10 %).

At Izaña HCN peaks in May–July due to the biomass burning activity occurring in northern America and Europe (Sancho et al., 1992). We find maxima of around 8 (6) $\times 10^{15}$ molec cm^{-2} in the IASI (ground-based FTIR) data set. The seasonality and interannual variability matches poorly with that of the ground-based FTIR measurements (correlation coefficient of 0.28 for the entire daily mean data set, and of 0.64 for the monthly mean data set), with the IASI columns being biased high by 0.45×10^{15} molec cm^{-2} (11 %). One can notice that HCN total columns as measured by ground-based FTIR are below the HCN stability threshold in boreal winter, which may result in erroneous IASI measurements (because unstable) and explain this poor match between the two data sets.

For C_2H_2 at the Jungfraujoch site, the agreement between IASI and the ground-based retrieved columns is good (correlation coefficient of 0.70 for the entire daily mean data set, and of 0.85 for the monthly mean data set), with the IASI columns being biased low by 0.15×10^{15} molec cm^{-2} (12 %), opposite to the observations at Reunion. The larger columns observed in late winter are caused by the increased C_2H_2 lifetime in that season (caused by the seasonal change in OH abundance) (Zander et al., 1991), and we find corresponding maxima of up to 4 (3) $\times 10^{15}$ molec cm^{-2} in the IASI (ground-based FTIR) data set.

3.2 IASI Global distributions

We focus in this section on the description of the C_2H_2 and HCN distributions retrieved from IASI spectra. For practical reasons, the figures used in this section also show simulated distributions that will be analyzed afterwards.

The left panels of Figs. 9 and 10 provide the seasonal global and subtropical distributions of C_2H_2 and HCN total columns, respectively, as measured by IASI and averaged over the years 2008 to 2010.

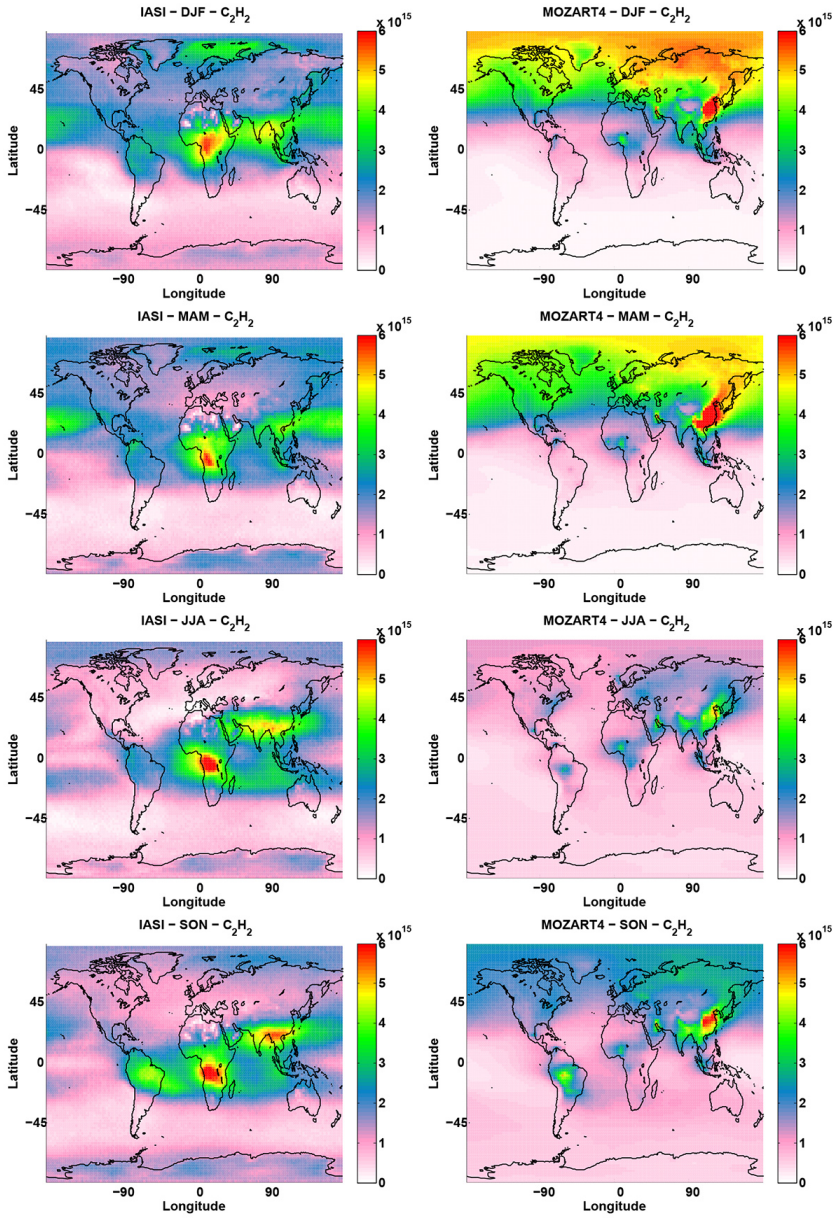

Figure 9. Seasonal distribution of the C_2H_2 total column (in molec cm^{-2}) as measured by IASI (left panel) and simulated by MOZART-4 (right panel) averaged over the years 2008 to 2010. The IASI global distributions are given with the same horizontal resolution as MOZART-4 (1.875° latitude × 2.5° longitude). DJF represents December–January–February, MAM: March–April–May, JJA: June–July–August, and SON: September–October–November.

Looking at IASI measurements (Figs. 9 and 10 – left panels), one can notice the following main persisting features for both C_2H_2 and HCN:

- the hot spots mainly due to the biomass burning activity occurring in Africa and moving southward along the year (Sauvage et al., 2005; van der Werf et al., 2006);
- the hot spot located in Southeast Asia being likely a combination of biomass burning and anthropogenic activities;
- the transatlantic transport pathway linking the African west coast to the South American east coast and moving southward along the year (Edwards et al., 2003, 2006a, b; Glatthor et al., 2015).

The following seasonal features can also be observed:

- the transpacific transport pathway linking eastern Asia to western North America, especially in March–April–May (MAM) (Yienger et al., 2000);

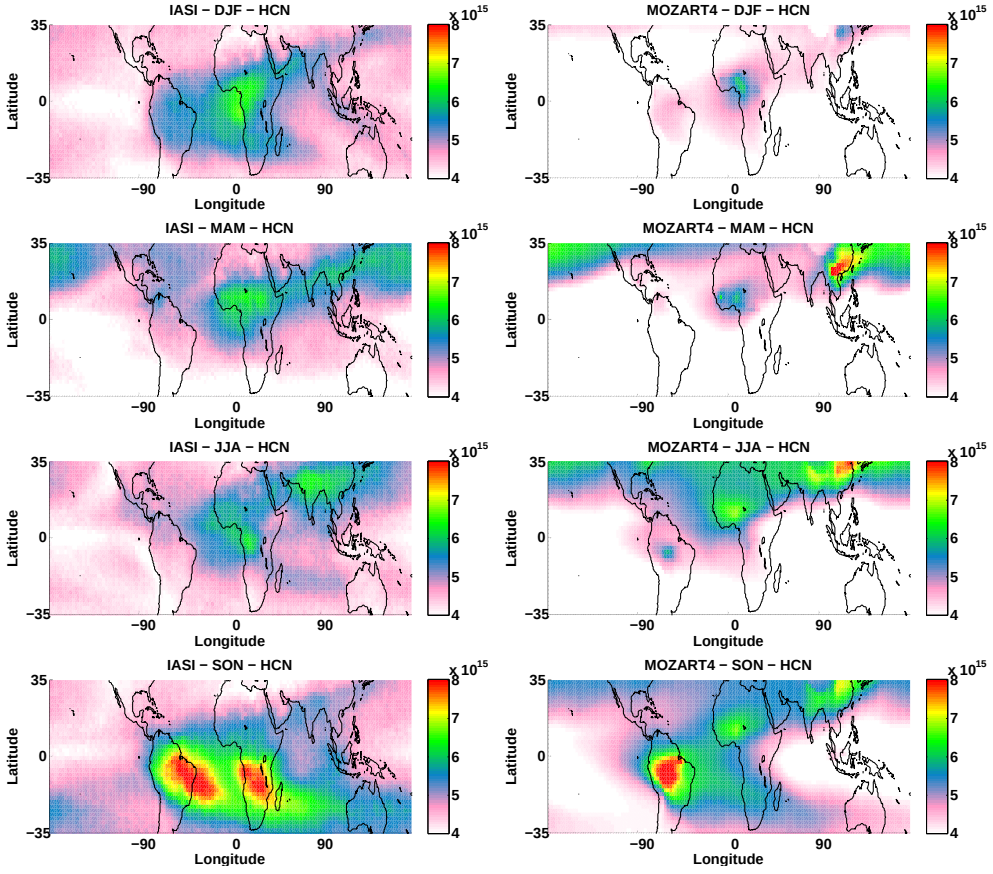

Figure 10. Same as Fig. 9 for HCN.

– the transport pathway from southern Africa to Australia in June–July–August (JJA) and September–October–November (SON) (Annegarn et al., 2002; Edwards et al., 2006a, b);

– the transport pathway linking South America (especially Amazonia) to southern Africa and Australia during the SON period (Edwards et al., 2006a, b; Glatthor et al., 2015);

– the transport of the northern African plume over southern Asia to as far as the eastern Pacific by the northern subtropical jet during the MAM period (Glatthor et al., 2015);

– the Asian monsoon anticyclone (AMA), which is the dominant circulation feature in the Indian–Asian upper troposphere–lower stratosphere (UTLS) region during the Asian summer monsoon, spanning Southeast Asia to the Middle East and flanked by the equatorial and subtropical jets (Hoskins and Rodwell, 1995). The AMA is a known region of persistent enhanced pollution in the upper troposphere, linked to rapid vertical transport of surface air from Asia, India, and Indonesia in deep convection, and confinement by the strong anticyclonic circulation (Randel et al., 2010). The enhanced abundance of C_2H_2 and HCN within the AMA in JJA observed by IASI is in accordance with previous studies (Park et al., 2008; Randel at al., 2010; Parker et al., 2011; Glatthor et al., 2015); however, one should keep in mind that this enhanced abundance measured by IASI is likely due to the combination of this pollution uplift and confinement with the higher sensitivity of the method in the upper troposphere (Fig. 2).

One can also notice the very good agreement between the seasonal HCN distributions shown in our Fig. 10 and the ones published recently in Glatthor et al. (2015, Fig. 3).

Figures 11 and 12 show the C_2H_2 and HCN total columns time series, respectively, as measured by IASI (red dots) with the associated standard deviation (light red lines) for each of the zones defined in Fig. 6.

In northern America, Europe and boreal Central Asia (Fig. 11 – zones NAM, EUR and BCA), C_2H_2 peaks in late boreal winter due to the increased C_2H_2 lifetime as already noticed over Jungfraujoch (Fig. 8). The boreal summer 2008 California wildfires event (Gyawali et al., 2009) is clearly visible in the NAM plot, as well as the August 2009 Russian

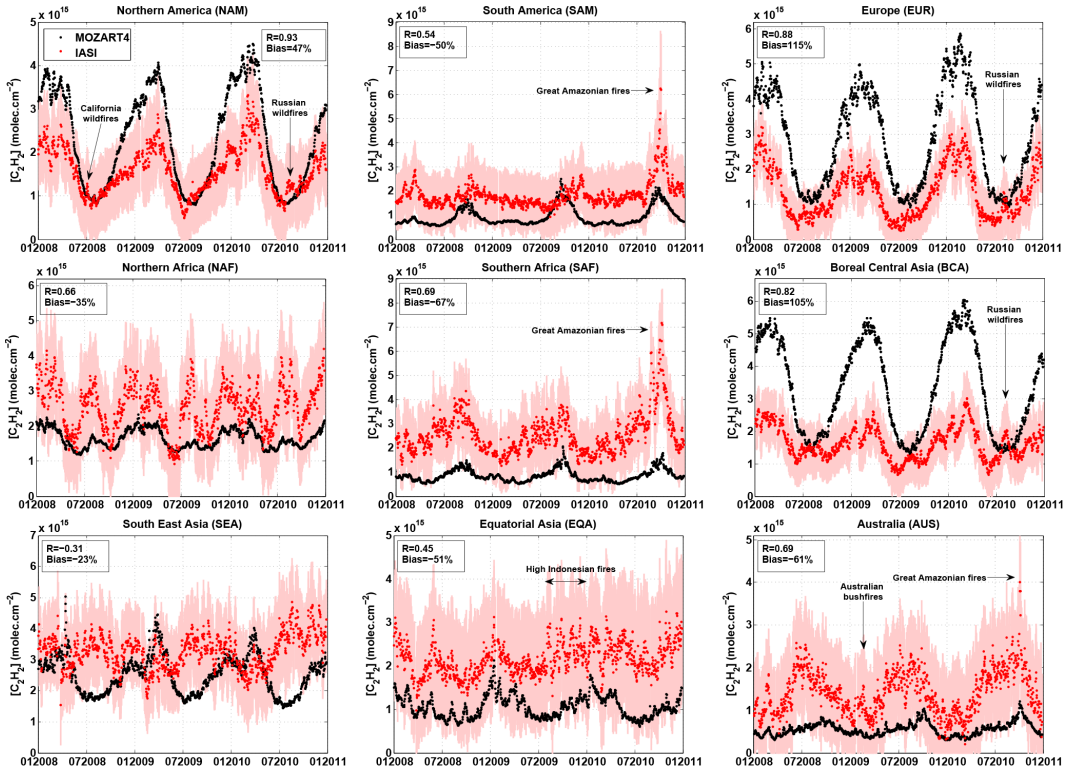

Figure 11. Evolution with time of the mean C_2H_2 total column (in molec cm^{-2}) over the zones defined in Fig. 6 as measured by IASI (red dots) with associated standard deviation (light red lines), and as simulated by MOZART-4 (black dots). Correlation coefficients (R) and biases (Bias) between IASI and MOZART-4 are given on each plot for daily means.

wildfires in the NAM, EUR and BCA plots (Parrington et al., 2012; R'Honi et al., 2013).

In north-central America (Fig. 12 – zone NCA), the annual HCN peak in April–June is driven by local fire activity (van der Werf et al., 2010).

In South America, southern Africa and Australia (Figs. 11 and 12 – zones SAM, SAF and AUS), the Southern Hemisphere biomass burning season clearly drives the C_2H_2 and HCN peaks in September–November each year. The signature of the great 2010 Amazonian fires (Lewis et al., 2011) is visible on each of the these three zones, South American fire plumes being known to impact southern Africa and Australia (Edwards et al., 2003, 2006a, b). The February 2009 Australian bush fires (Glatthor et al., 2013) are also noticeable on zone AUS for both species.

In northern Africa (Figs. 11 and 12 – zone NAF), C_2H_2 and HCN peak in boreal winter because of the biomass burning activity occurring in the zone, and peak also in boreal summer because of the European and southern Mediterranean fires (van der Werf et al., 2010).

In Southeast Asia (Figs. 11 and 12 – zone SEA), the observed C_2H_2 and HCN peaks in July–September and January–March are due to local fire activity (Fortems-Cheiney et al., 2011; Magi et al., 2012). Additionally, the July–September peaks are also likely due to the combination of the pollution uplift and confinement within the AMA with the higher sensitivity of the method in the upper troposphere.

In equatorial Asia (Figs. 11 and 12 – zone EQA), local fire activity is visible in July–October, as well as the Southeast Asian fire activity in January–March (Fortems-Cheiney et al., 2011; Magi et al., 2012). The high biomass burning activity occurring in Indonesia from July to December 2009 (Yulianti et al., 2013; Hyer et al., 2013) is also clearly noticeable.

C_2H_2 and HCN sharing important common sources (cf. Introduction), the same annual and seasonal features are observed for both species. However, biomass burning being the major source for HCN (while it is biofuel and fossil fuel combustions for C_2H_2), one can notice the especially high increase in HCN abundance (up to 13×10^{15} molec cm^{-2}) in the Southern Hemisphere during the austral biomass burning season (September to November). These observations are in accordance with previous studies (Lupu et al, 2009; Glatthor et al., 2009; Wiegele et al., 2012).

3.3 Comparison with model

In order to further evaluate the HCN and C_2H_2 distributions retrieved from IASI spectra, they are compared in this section to the output of MOZART-4 for the years 2008–2010. We first describe the simulation set-up before comparing simu-

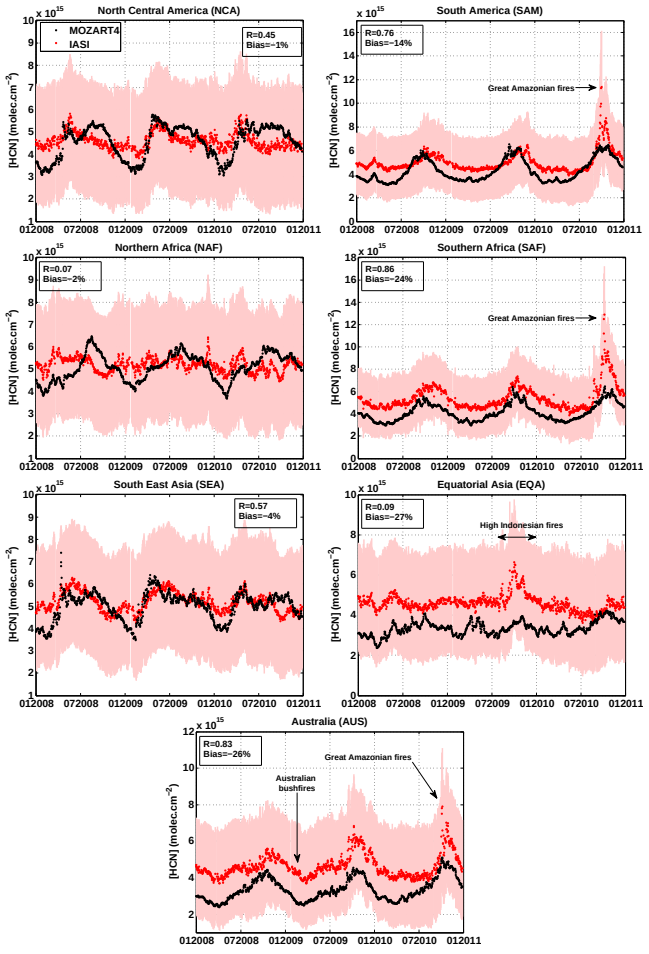

Figure 12. Same as Fig. 11 for HCN.

lated abundances with the ground-based observations at the four sites already studied in Sect. 3.1. We finally compare the simulated and observed global distributions.

3.3.1 MOZART-4 simulation set-up

The model simulations presented here are performed with the MOZART-4 global 3-D chemical transport model (Emmons et al., 2010a), which is driven by assimilated meteorological fields from the NASA Global Modeling and Assimilation Office (GMAO) Goddard Earth Observing System (GEOS). MOZART-4 was run with a horizontal resolution of 1.875° latitude × 2.5° longitude, with 56 levels in the vertical and with its standard chemical mechanism (see Emmons et al. (2010a) and Lamarque et al. (2012), for details). The model simulations have been initialized by simulations starting in July 2007 to avoid contamination by the spin-up in the model results. MOZART-4 simulations of numerous species (CO, O_3 and related tracers including C_2H_2 and HCN) have been previously compared to in situ and satellite observations and used to track the intercontinental transport of pollution (e.g. Emmons et al., 2010b; Pfister et al., 2006, 2008, 2011; Tilmes et al., 2011; Clarisse et al., 2011b; Wespes et al., 2012; Viatte et al., 2015).

Table 2. Global C_2H_2 and HCN emission sources (Tg(species) yr^{-1}) during the period 2008–2010 from the data set used in MOZART-4.

	C_2H_2			HCN		
Sources yr^{-1}	2008	2009	2010	2008	2009	2010
Anthropogenic	3.37	3.37	3.37	1.67	1.67	1.67
Biomass burning	0.64	0.71	0.83	1.38	1.33	1.58
Total	4.01	4.07	4.20	3.05	3.00	3.25

The surface anthropogenic (including fossil fuel and biofuel) emissions used here were taken from the inventory provided by D. Streets and University of Iowa and created for the Arctic Research of the Composition of the Troposphere from Aircraft and Satellites (ARCTAS) campaign (see http://bio.cgrer.uiowa.edu/arctas/emission.html for more information). This inventory was developed in the frame of the POLARCAT Model Intercomparison Program (POLMIP) and is a composite data set of regional emissions as representative of current emissions as possible; it is built upon the INTEX-B Asia inventory (Zhang et al., 2009) with the US NEI (National Emission Inventory) 2002 and CAC 2005 for North America and the EMEP (European Monitoring and Evaluation Programme) 2006 for Europe inventory to make up NH emissions (see Emmons et al. (2015) for an evaluation of POLMIP models). Emissions from EDGAR (Emissions Database for Global Atmospheric Research) were used for missing regions and species. Since only total volatile organic compounds (VOCs) were provided with this POLMIP inventory, the VOC speciation based on the RETRO emissions inventory as in Lamarque et al. (2010) was used. The anthropogenic emissions are constant in time with no monthly variations.

Daily biomass burning emissions were taken from the global Fire INventory from NCAR (FINN) version 1 (Wiedinmyer et al., 2011). The fire emissions for individual fires, based on daily MODIS fire counts, were calculated and then gridded to the simulation resolution (Wiedinmyer et al., 2006, 2011). The oceanic emissions are taken from the POET emissions data set (Granier et al., 2005) and the biogenic emissions from MEGANv2 (Model of Emissions of Gases and Aerosols from Nature) data set inventory (Guenther et al., 2006).

Model emissions for HCN and C_2H_2 used in this study are summarized in Table 2 and presented in Fig. 13. The majority of the emissions for both C_2H_2 and HCN are from anthropogenic source (about 80 and 55 % of the global source of C_2H_2 and HCN, respectively; see Table 2). Averaged over the period 2008–2010, the highest HCN and C_2H_2 anthropogenic surface emissions are observed over China, with elevated emissions over India, Europe and USA, due to in-

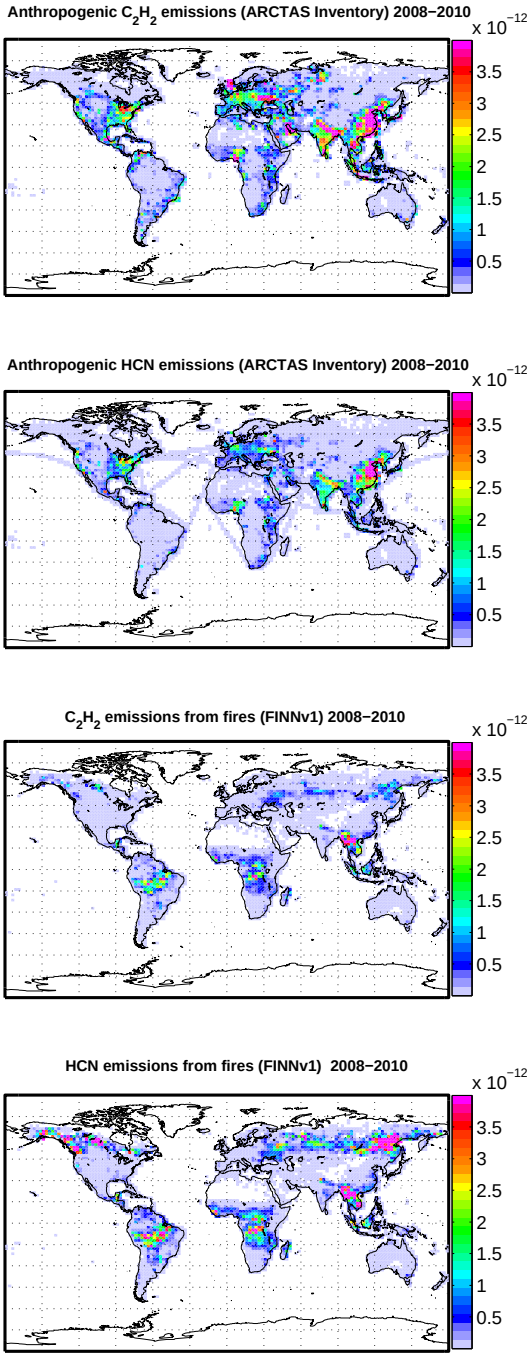

Figure 13. C_2H_2 and HCN surface emission fluxes ($kg\,m^{-2}\,s^{-1}$) averaged over the period 2008–2010 from the anthropogenic and fire emissions inventories used in MOZART-4.

tense industrialization, where values larger than 4×10^{-12} $kg(C_2H_2)\ m^{-2}\,s^{-1}$ are entered in the model. The most intense HCN and C_2H_2 emissions due to biomass burning are observed over Southeast Asia, equatorial and southern Africa, South America, Siberia and Canada.

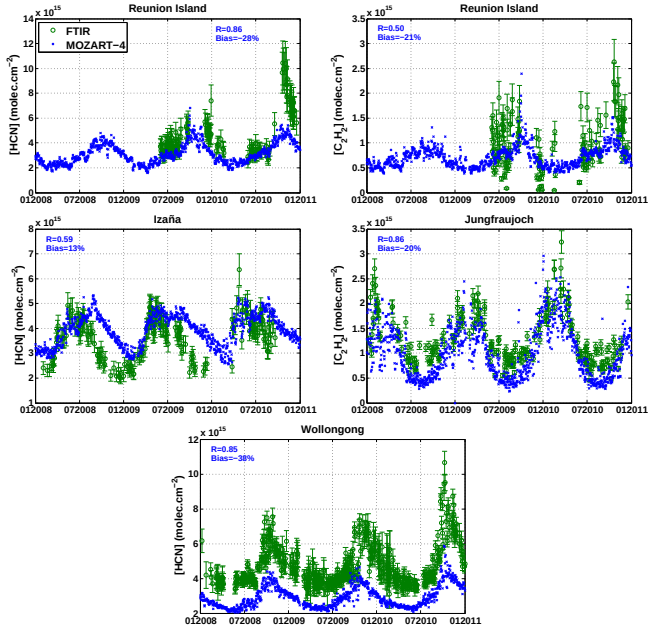

Figure 14. Time series of HCN (left panel) and C_2H_2 (right panel) measurements and simulations for Reunion Island (HCN and C_2H_2), Wollongong (HCN only), Izaña (HCN only), and Jungfraujoch (C_2H_2 only). MOZART-4 total columns are shown as daily and $1.875° \times 2.5°$ means (blue crosses). Ground-based FTIR measurements are shown as daily means with associated total error by green circles and lines. Correlation coefficient and bias are given on each plot for daily means.

3.3.2 Model vs. ground-based FTIR observations

MOZART-4 simulations can be first evaluated by comparing them to the ground-based measurements at the four sites studied previously (Sect. 3.1). To perform this comparison, we use the FTIR averaging kernels and a priori to degrade the model vertical profile to the FTIR vertical resolution, in order to obtain the model "smoothed" total column, which represents what the FTIR would measure if the model profile was the true state (see Eq. (25) of Rodgers and Connor (2003), and Vigouroux et al. (2012) for an example). Figure 14 shows the comparison between the simulated "smoothed" total columns and the ground-based measurements. Model outputs are given in a $1.875°$ latitude $\times$ $2.5°$ longitude box (corresponding to the horizontal resolution of the model) over the ground-based measurement points. One can see that there is an overall agreement between the ground-based instruments and the model, the latter being obviously able to capture the seasonality in the two species in most of the cases.

For HCN, the model seasonality and interannual variability matches the ground-based FTIR measurements at Reunion Island very well (correlation coefficient of 0.86) and Wollongong (correlation coefficient of 0.85), and reasonably well at Izaña (correlation coefficient of 0.59). For this last site, one can see that the model correctly captures the abun-

dance peak occurring in May–July (cf. Sect. 3.1), but sets another peak around October. This second yearly peak for HCN at Izaña in the model simulations could be due to an overestimation of the southern African contribution to the northern African loading; this hypothesis will be analyzed in the next section. For HCN, the simulated total columns are biased low at Reunion Island by 1.29×10^{15} molec cm^{-2} (28 %) and at Wollongong by 1.8×10^{15} molec cm^{-2} (38 %). One can notice that the model does not capture the 2010 great Amazonian fires exceptional event visible on ground-based measurements at Reunion Island and Wollongong (cf. Sect. 3.1), which could explain the biases between the model and ground-based data sets at these two sites. At Izaña, the model is biased high by 0.46×10^{15} molec cm^{-2} (13 %), which seems to be caused by the second yearly peak simulated by the model.

For C_2H_2, the model seasonality and interannual variability matches very well that of the ground-based FTIR measurements at Jungfraujoch (correlation coefficient of 0.86) and reasonably well at Reunion Island (correlation coefficient of 0.50). For this last site, one can see that the model captures correctly the yearly peak occurring in October–November (cf. Sect. 3.1), but struggles to simulate the large day-to-day variations observed by the ground-based FTIR. This is illustrated by the very good correlation coefficient between the two data sets when dealing with monthly mean observations: 0.87 (data not shown). For C_2H_2, the simulated total columns are biased low for every sites: 0.20×10^{15} molec cm^{-2} (21 %) at Reunion Island, and 0.27×10^{15} molec cm^{-2} (20 %) at Jungfraujoch. Similar to HCN, one can notice that the model does not capture the 2010 great Amazonian fires exceptional event visible on ground-based measurements at Reunion Island, which could explain the bias between the model and ground-based data sets at this site.

3.3.3 IASI vs. model global distributions

Figures 9 and 10 provide the seasonal global and subtropical distributions of C_2H_2 and HCN total columns, respectively, as measured by IASI and as simulated by MOZART-4 averaged over the years 2008 to 2010. For comparisons with IASI, the hourly output from MOZART-4 was interpolated to the overpass time of IASI. In addition, the high-resolution modelled layers were smoothed by applying each of the MOZART-4 simulated profiles, the Jacobians of the used forward model (cf. Sects. 2.2.3 and Fig. 3), to take into account the sensitivity of both the radiative transfer model and IASI. This has been done instead of applying the averaging kernels since our retrieval scheme does not provide such information. Note that here again HCN abundances below 2.8×10^{15} molec cm^{-2} have been removed from both space measurements and simulated columns to allow for comparison of both data sets (cf. Sect. 2.2.3).

Table 3. Correlation coefficients (R) and biases (Bias) between IASI observations and MOZART-4 simulations for each of the zones defined in Fig. 6.

	C_2H_2		HCN	
Zones	R	Bias (%)	R	Bias (%)
NAM	0.93	47		
NCA			0.44	−1
SAM	0.54	−50	0.76	−14
EUR	0.88	115		
NAF	0.66	−35	0.07	−2
SAF	0.69	−67	0.86	−28
BCA	0.82	105		
SEA	−0.31	−23	0.57	−4
EQA	0.45	−51	0.09	−27
AUS	0.65	−61	0.77	−26
Global	0.72	−1	0.69	−16

MOZART-4 simulations can be evaluated by looking at Figs. 9 and 11 for C_2H_2, and Figs. 10 and 12 for HCN. Figures 11 and 12 show the simulated C_2H_2 and HCN total columns time series, respectively, for each of the zones defined in Fig. 6 superimposed to IASI observations. Table 3 summarizes the biases and correlation coefficients resulting from the comparison between model and observations. Looking at these tables and figures, the following conclusions can be drawn:

- Seasonal cycles observed from satellite data are reasonably well reproduced by the model.
- The African, South American, Asian and Indonesian hot spots are clearly visible in the model.
- Exceptional events that are captured by IASI (cf. Sect. 3.2) are not simulated by MOZART-4.
- The model is more negatively biased in the Southern Hemisphere (bias = −61 % for C_2H_2 and bias = -25 % for HCN) than in the Northern Hemisphere (bias = 40 % for C_2H_2 and bias = −3 % for HCN), suggesting that anthropogenic (biomass burning) emissions are likely overestimated (underestimated) in the model. Note that in the MOZART-4 simulation presented here, the fire emissions are injected at the surface, which might result in an underestimation of concentrations at higher altitudes where IASI shows an increased sensitivity.
- The model reasonably reproduces the main transport pathways identified on IASI observations (cf. Sect. 3.2). However, the low background concentrations in the Southern Hemisphere as simulated by the model, especially for southern Africa and Australia (Figs. 11 and 12 – zones SAF and AUS and previous section at Reunion

Island and Wollongong), is possibly due to a mix of uncertainties introduced by the coarse grid of the model producing too much diffusion, problems in the transportation scheme for fine-scale plumes, the fire injection set at the surface and uncertainties in the emissions. The fact that only three representative Jacobians are used to perform the global comparison might also play a role.

In Table 3, for C_2H_2, the correlation coefficients are good (≥ 0.6) to very good (≥ 0.9) except for the zones SAM (South America), SEA (Southeast Asia) and EQA (equatorial Asia). For HCN, the correlation coefficients are good (≥ 0.6) except for the zones NCA (north-central America), NAF (northern Africa), SEA and EQA.

For South America (zone SAM), correlation coefficient is not as good for C_2H_2 ($R = 0.54$) due to a backward shift of the species abundance peaks in years 2008 and 2009: in the model, this increase occurs from July to October, while observations (and previous studies, e.g. van der Werf et al., 2010) show an increase from August to December. This backward shift is also visible for HCN (Fig. 12), but to a lesser extent.

For Southeast Asia and equatorial Asia (zones SEA and EQA), the low correlation coefficients (cf. Table 3) can be attributed to the difficulty of locating precisely with the model the intercontinental convergence zone (ITCZ) which drives the long-range transport of C_2H_2 and HCN-loaded plumes into the zone. Moreover, for Southeast Asia, the very low correlation coefficient for C_2H_2 (-0.31) may be caused by (i) the model setting the high abundance peaks in DJF and MAM (Fig. 9, especially visible over China coast, and Fig. 11), which may be due to an overestimation of the Asian anthropogenic emissions, and (ii) IASI observations exhibiting July–September peaks, which are likely due to the combination of the pollution uplift and confinement within the AMA with the higher sensitivity of the method in the upper troposphere. Additionally, for equatorial Asia, the too low fire emissions considered in the model for Indonesia from July to December 2009 may also be a cause for these low correlation coefficients.

For HCN in northern Africa (zone NAF), correlation coefficient is very low ($R = 0.07$) because the model sets the abundance peaks around August while observations show peaks occurring around December, which is in accordance with previous studies (van der Werf et al., 2010). This inadequate timing for HCN in the model simulations could be due to an overestimation of the southern African contribution to the northern African loading and is visible on Fig. 10 (JJA).

4 Conclusions

We have presented a fast method to retrieve HCN and C_2H_2 total columns from IASI spectra. The sensitivity of this method to the two species is mostly in the mid-upper troposphere. With this method, C_2H_2 total columns can be retrieved globally with 5 % precision, while HCN abundances can be retrieved for abundances greater than 0.28×10^{16} molec cm^{-2} with 10 % precision in the $\pm 20°$ latitudinal band and with 25 % precision in the $[\pm 35° : \pm 20°]$ latitudinal band.

Total columns have been retrieved globally for a 3-year period and compared to routine FTIR measurements available at Reunion Island (HCN and C_2H_2), Wollongong (HCN), Jungfraujoch (C_2H_2), and Izaña (HCN). The comparison between IASI and FTIR retrieved total columns demonstrates the capabilities of IASI to capture the seasonality in HCN and C_2H_2 in most cases.

Global seasonal distributions, as well as regional time series of the total columns, have been shown for the two species. IASI is able to capture persisting, seasonal and exceptional features for both species, and the observed patterns are in a general good agreement with previous spaceborne studies (ACE-FTIR and MIPAS).

The comparison between MOZART-4 simulations and the ground-based FTIR measurements, together with the comparison between the IASI observations and MOZART-4 simulations leads to the following conclusions: (i) the model is able to capture most of the hot spots and seasonal cycles, but not the exceptional events; (ii) the anthropogenic (biomass burning) emissions used in the model seem to be overestimated (underestimated) for both species; (iii) discrepancies between simulations and observations are most probably due to the coarse grid of the model producing too much diffusion and problems in the transportation scheme for fine-scale plumes, as well as to the fire injection set at the surface.

Acknowledgements. IASI has been developed and built under the responsibility of the Centre National d'Etudes Spatiales (CNES, France). It is flown onboard the MetOp satellites as part of the EUMETSAT Polar System. The IASI L1 data are received through the EUMETCast near-real-time data distribution service. Part of the research is supported by EUMETSAT through the O3SAF project. P.-F. Coheur is Senior Research Associate and L. Clarisse is Research Associate at the F.R.S.-FNRS. The research in Belgium was funded by the F.R.S.-FNRS, the Belgian Science Policy Office, and the European Space Agency (ESA Prodex arrangements and the AGACC-II project). The Australian Research Council has provided financial support over the years for the NDACC site at Wollongong, most recently as part of project DP110101948. The Liège team further acknowledges the Fédération Wallonie-Bruxelles for supporting travel costs to the Jungfraujoch station and wishes to thank the International Foundation High Altitude Research Stations Jungfraujoch and Gornergrat (HFSJG, Bern) for supporting the facilities needed to perform the observations. Since 1999, the Izaña FTIR activities have been supported by different funding agencies: European Commission, European Research Council, European Space Agency, EUMETSAT, Deutsche Forschungsgemeinschaft, Deutsches Zentrum für Luft- und Raumfahrt, and the Ministerios de Ciencia e Innovación and Educación from Spain. The authors also wish to thank the French regional, national (INSU, CNRS), and international (NASA/GFSC) organizations for supporting the

OPAR (Observatoire de Physique de l'Atmosphère de la Réunion) station. The NDACC is also acknowledged for providing consistent and well-documented data sets.

Edited by: P. Monks

References

Anderson, G. P., Clough, S. A., Kneizys, F. X., Chetwynd, J. H., and Shettle, E. P.: AFGL Atmospheric Constituent Profiles (0–120 km), Environmental Research Papers no. 954, Air Force Geophysics Laboratory, Hanscom AFB Massachusetts, AFGL TR-86-0110, 1986.

Annegarn, H. J., Otter, L., Swap, R. J., and Scholes, R. J.: Southern Africas ecosystem in a test-tube-A perspective on the Southern African Regional Science Initiative (SAFARI 2000), S. Afr. J. Sci., 98, 111–113, 2002.

Clarisse, L., Coheur, P. F., Prata, A. J., Hurtmans, D., Razavi, A., Phulpin, T., Hadji-Lazaro, J., and Clerbaux, C.: Tracking and quantifying volcanic SO2 with IASI, the September 2007 eruption at Jebel at Tair, Atmos. Chem. Phys., 8, 7723–7734, doi:10.5194/acp-8-7723-2008, 2008.

Clarisse L., Clerbaux C., Dentener F., Hurtmans D., and Coheur P.-F.: Global ammonia distribution derived from infrared satellite observations, Nat. Geosci., 2, 479–483, doi:10.1038/NGEO551, 2009.

Clarisse, L., R'Honi, Y., Coheur, P.-F., Hurtmans, D., and Clerbaux, C.: Thermal infrared nadir observations of 24 atmospheric gases, Geophys. Res. Lett., 38, L10802, doi:10.1029/2011GL047271, 2011a.

Clarisse, L., Formm, M., Ngadi, Y., Emmons, L., Clerbaux, C., Hurtmans, D., and Coheur, P. F.: Intercontinental transport of anthropogenic sulfur dioxide and other pollutants: An infrared remote sensing case study, Geophys. Res. Lett., 38, L19806, doi:10.1029/2011GL048976, 2011b.

Clerbaux, C., Boynard, A., Clarisse, L., George, M., Hadji-Lazaro, J., Herbin, H., Hurtmans, D., Pommier, M., Razavi, A., Turquety, S., Wespes, C., and Coheur, P.-F.: Monitoring of atmospheric composition using the thermal infrared IASI/MetOp sounder, Atmos. Chem. Phys., 9, 6041–6054, doi:10.5194/acp-9-6041-2009, 2009.

Coheur, P.-F., Barret, B., Turquety, S., Hurtmans, D., Hadji-Lazaro, J., and Clerbaux, C.: Retrieval and characterization of ozone vertical profiles from a thermal infrared nadir sounder, J. Geophys. Res., 110, D24303, doi:10.1029/2005JD005845, 2005.

Duflot, V., Dils, B., Baray, J. L., De Maziére, M., Attié, J. L., Vanhaelewyn, G., Senten, C., Vigouroux, C., Clain, G., and Delmas, R.: Analysis of the origin of the distribution of CO in the subtropical southern Indian Ocean in 2007, J. Geophys. Res., 115, D22106, doi:10.1029/2010JD013994, 2010.

Duflot, V., Hurtmans, D., Clarisse, L., R'honi, Y., Vigouroux, C., De Mazière, M., Mahieu, E., Servais, C., Clerbaux, C., and Coheur, P.-F.: Measurements of hydrogen cyanide (HCN) and acetylene (C_2H_2) from the Infrared Atmospheric Sounding Interferometer (IASI), Atmos. Meas. Tech., 6, 917–925, doi:10.5194/amt-6-917-2013, 2013.

Edwards D. P., Lamarque, J.-F., Attié, J.-L., Emmons, L. K., Richter, A., Cammas, J.-P., Gille, J. C., Francis, G. L., Deeter, M. N., Warner, J., Ziskin, D. C., Lyjak, L. V., Drummond, J. R., and Burrows, J. P.: Tropospheric ozone over the tropical Atlantic: A satellite perspective, J. Geophys. Res., 108, 4237, doi:10.1029/2002JD002927, 2003.

Edwards, D. P., Emmons, L. K., Gille, J. C., Chu, A., Attié, J.-L., Giglio, L., Wood, S. W., Haywood, J., Deeter, M. N., Massie, S. T., Ziskin, D. C., and Drummond, J. R.: Satellite-observed pollution from Southern Hemisphere biomass burning, J. Geophys. Res., 111, D14312, doi:10.1029/2005JD006655, 2006a.

Edwards, D. P., Emmons, L. K., Gille, J. C., Chu, A., Attié, J.-L., Giglio, L., Wood, S. W., Haywood, J., Deeter, M. N., Massie, S. T., Ziskin, D. C., and Drummond J. R.: Satellite-observed pollution from Southern Hemisphere biomass burning, J. Geophys. Res., 111, D14312, doi:10.1029/2005JD006655, 2006b.

Emmons, L. K., Walters, S., Hess, P. G., Lamarque, J.-F., Pfister, G. G., Fillmore, D., Granier, C., Guenther, A., Kinnison, D., Laepple, T., Orlando, J., Tie, X., Tyndall, G., Wiedinmyer, C., Baughcum, S. L., and Kloster, S.: Description and evaluation of the Model for Ozone and Related chemical Tracers, version 4 (MOZART-4), Geosci. Model Dev., 3, 43–67, doi:10.5194/gmd-3-43-2010, 2010a.

Emmons, L. K., Apel, E. C., Lamarque, J.-F., Hess, P. G., Avery, M., Blake, D., Brune, W., Campos, T., Crawford, J., DeCarlo, P. F., Hall, S., Heikes, B., Holloway, J., Jimenez, J. L., Knapp, D. J., Kok, G., Mena-Carrasco, M., Olson, J., O'Sullivan, D., Sachse, G., Walega, J., Weibring, P., Weinheimer, A., and Wiedinmyer, C.: Impact of Mexico City emissions on regional air quality from MOZART-4 simulations, Atmos. Chem. Phys., 10, 6195–6212, doi:10.5194/acp-10-6195-2010, 2010b.

Emmons, L. K., Arnold, S. R., Monks, S. A., Huijnen, V., Tilmes, S., Law, K. S., Thomas, J. L., Raut, J.-C., Bouarar, I., Turquety, S., Long, Y., Duncan, B., Steenrod, S., Strode, S., Flemming, J., Mao, J., Langner, J., Thompson, A. M., Tarasick, D., Apel, E. C., Blake, D. R., Cohen, R. C., Dibb, J., Diskin, G. S., Fried, A., Hall, S. R., Huey, L. G., Weinheimer, A. J., Wisthaler, A., Mikoviny, T., Nowak, J., Peischl, J., Roberts, J. M., Ryerson, T., Warneke, C., and Helmig, D.: The POLARCAT Model Intercomparison Project (POLMIP): overview and evaluation with observations, Atmos. Chem. Phys., 15, 6721–6744, doi:10.5194/acp-15-6721-2015, 2015.

Fortems-Cheiney, A., Chevallier, F., Pison, I., Bousquet, P., Szopa, S., Deeter, M. N., and Clerbaux, C.: Ten years of CO emissions as seen from Measurements of Pollution in the Troposphere (MOPITT), J. Geophys. Res., 116, D05304, doi:10.1029/2010JD014416, 2011.

Glatthor, N., von Clarmann, T., Stiller, G. P., Funke, B., Koukouli, M. E., Fischer, H., Grabowski, U., Höpfner, M., Kellmann, S., and Linden, A.: Large-scale upper tropospheric pollution observed by MIPAS HCN and C_2H_6 global distributions, Atmos. Chem. Phys., 9, 9619–9634, doi:10.5194/acp-9-9619-2009, 2009.

Glatthor, N., Höpfner, M., Semeniuk, K., Lupu, A., Palmer, P. I., McConnell, J. C., Kaminski, J. W., von Clarmann, T., Stiller, G. P., Funke, B., Kellmann, S., Linden, A., and Wiegele, A.: The Australian bushfires of February 2009: MIPAS observations and GEM-AQ model results, Atmos. Chem. Phys., 13, 1637–1658, doi:10.5194/acp-13-1637-2013, 2013.

Glatthor, N., Höpfner, M., Stiller, G. P., von Clarmann, T., Funke, B., Lossow, S., Eckert, E., Grabowski, U., Kellmann, S., Linden,

A., A. Walker, K., and Wiegele, A.: Seasonal and interannual variations in HCN amounts in the upper troposphere and lower stratosphere observed by MIPAS, Atmos. Chem. Phys., 15, 563–582, doi:10.5194/acp-15-563-2015, 2015.

González Abad, G., Allen, N. D. C., Bernath, P. F., Boone, C. D., McLeod, S. D., Manney, G. L., Toon, G. C., Carouge, C., Wang, Y., Wu, S., Barkley, M. P., Palmer, P. I., Xiao, Y., and Fu, T. M.: Ethane, ethyne and carbon monoxide concentrations in the upper troposphere and lower stratosphere from ACE and GEOS-Chem: a comparison study, Atmos. Chem. Phys., 11, 9927–9941, doi:10.5194/acp-11-9927-2011, 2011.

Granier, C., Lamarque, J., Mieville, A., Müller, J., Olivier, J., Orlando, J., Peters, J., Petron, G., Tyndall, G., and Wallens, S.: POET, a database of surface emissions of ozone precursors, available at: http://www.pole-ether.fr/eccad (last access: 22 September 2015), 2005.

Guenther, A., Karl, T., Harley, P., Wiedinmyer, C., Palmer, P. I., and Geron, C.: Estimates of global terrestrial isoprene emissions using MEGAN (Model of Emissions of Gases and Aerosols from Nature), Atmos. Chem. Phys., 6, 3181–3210, doi:10.5194/acp-6-3181-2006, 2006.

Gyawali, M., Arnott, W. P., Lewis, K., and Moosmüller, H.: In situ aerosol optics in Reno, NV, USA during and after the summer 2008 California wildfires and the influence of absorbing and non-absorbing organic coatings on spectral light absorption, Atmos. Chem. Phys., 9, 8007–8015, doi:10.5194/acp-9-8007-2009, 2009.

Hoskins, B. J. and M. J. Rodwell: A model of the Asian summer monsoon. Part I: the global scale, J. Atmos. Sci., 52, 1329–1340, 1995.

Hyer E. J., Reid, J. S., Prins, E. M., Hoffman, J. P., Schmidt, C. C., Miettinen, J. I., and Giglio, L.: Patterns of fire activity over Indonesia and Malaysia from polar and geostationary satellite observations, Atmos. Res., 122, 504–519, 2013.

Lamarque, J.-F., Bond, T. C., Eyring, V., Granier, C., Heil, A., Klimont, Z., Lee, D., Liousse, C., Mieville, A., Owen, B., Schultz, M. G., Shindell, D., Smith, S. J., Stehfest, E., Van Aardenne, J., Cooper, O. R., Kainuma, M., Mahowald, N., McConnell, J. R., Naik, V., Riahi, K., and van Vuuren, D. P.: Historical (1850–2000) gridded anthropogenic and biomass burning emissions of reactive gases and aerosols: methodology and application, Atmos. Chem. Phys., 10, 7017–7039, doi:10.5194/acp-10-7017-2010, 2010.

Lamarque, J.-F., Emmons, L. K., Hess, P. G., Kinnison, D. E., Tilmes, S., Vitt, F., Heald, C. L., Holland, E. A., Lauritzen, P. H., Neu, J., Orlando, J. J., Rasch, P. J., and Tyndall, G. K.: CAM-chem: description and evaluation of interactive atmospheric chemistry in the Community Earth System Model, Geosci. Model Dev., 5, 369–411, doi:10.5194/gmd-5-369-2012, 2012.

Lewis S. L., Brando, P. M., Phillips, O. L., van der Heijden, G. M. F., and Nepstad, D.: The 2010 Amazon Drought, Science, 331, p. 554, doi:10.1126/science.1200807, 2011.

Li, Q., Jacob, D., Bey, I., Yantosca, R., Zhao, Y., Kondo, Y., and Notholt, J.: Atmospheric hydrogen cyanide (HCN): Biomass burning source, ocean sink?, Geophys. Res. Lett., 27, 357–360, 2000.

Li, Q., Jacob, D. J., Yantosca, R. M., Heald, C. L., Singh, H. B., Koike, M., Zhao, Y., Sachse, G. W., and Streets, D. G.: A global three-dimensional model analysis of the atmospheric budgets of HCN and CH_3CN: Constraints from aircraft and ground measurements, J. Geophys. Res., 108, 8827, doi:10.1029/2002JD003075, 2003.

Li, Q., Palmer, P. I., Pumphrey, H. C., Bernath, P., and Mahieu, E.: What drives the observed variability of HCN in the troposphere and lower stratosphere?, Atmos. Chem. Phys., 9, 8531–8543, doi:10.5194/acp-9-8531-2009, 2009.

Logan, J. A., Prather, M. J., Wofsy, S. C., and McElroy, M. B.: Tropospheric chemistry: A global perspective, J. Geophys. Res., 86, 7210–7254, 1981.

Lupu, A., Kaminski, J. W., Neary, L., McConnell, J. C., Toyota, K., Rinsland, C. P., Bernath, P. F., Walker, K. A., Boone, C. D., Nagahama, Y., and Suzuki, K.: Hydrogen cyanide in the upper troposphere: GEM-AQ simulation and comparison with ACE-FTS observations, Atmos. Chem. Phys., 9, 4301–4313, doi:10.5194/acp-9-4301-2009, 2009.

Magi, B. I., Rabin, S., Shevliakova, E., and Pacala, S.: Separating agricultural and non-agricultural fire seasonality at regional scales, Biogeosciences, 9, 3003–3012, doi:10.5194/bg-9-3003-2012, 2012.

Mahieu, E., Duchatelet, P., Bernath, P. F., Boone, C. D., De Mazière, M., Demoulin, P., Rinsland, C. P., Servais, C., and Walker, K. A.: Retrievals of C_2H_2 from high-resolution FTIR solar spectra recorded at the Jungfraujoch station (46.5° N) and comparison with ACE-FTS observations, Geophys. Res. Abstract, 10, http://hdl.handle.net/2268/15191 (last access: 23 September 2015), 2008.

Park, M., Randel, W. J., Emmons, L. K., Bernath, P. F., Walker, K. A., and Boone, C. D.: Chemical isolation in the Asian monsoon anticyclone observed in Atmospheric Chemistry Experiment (ACE-FTS) data, Atmos. Chem. Phys., 8, 757–764, doi:10.5194/acp-8-757-2008, 2008.

Parker, R. J., Remedios, J. J., Moore, D. P., and Kanawade, V. P.: Acetylene C_2H_2 retrievals from MIPAS data and regions of enhanced upper tropospheric concentrations in August 2003, Atmos. Chem. Phys., 11, 10243–10257, doi:10.5194/acp-11-10243-2011, 2011.

Parrington, M., Palmer, P. I., Henze, D. K., Tarasick, D. W., Hyer, E. J., Owen, R. C., Helmig, D., Clerbaux, C., Bowman, K. W., Deeter, M. N., Barratt, E. M., Coheur, P.-F., Hurtmans, D., Jiang, Z., George, M., and Worden, J. R.: The influence of boreal biomass burning emissions on the distribution of tropospheric ozone over North America and the North Atlantic during 2010, Atmos. Chem. Phys., 12, 2077–2098, doi:10.5194/acp-12-2077-2012, 2012.

Paton-Walsh, C., Deutscher, N. M., Griffith, D. W. T., Forgan, B. W., Wilson, S. R., Jones, N. B., and Edwards, D. P.: Trace gas emissions from savanna fires in northern Australia, J. Geophys. Res., 115, D16314, doi:10.1029/2009JD013309, 2010.

Pfister, G. G., Emmons, L. K., Hess, P. G., Honrath, R., Lamarque, J.-F., Val Martin, M., Owen, R. C., Avery, M. A., Browell, E. V., Holloway, J. S., Nédélec, P., Purvis, R., Ryerson, T. B., Sachse, G. W., and Schlager, H.: Ozone production from the 2004 North American boreal fires, J. Geophys. Res., 111, D24S07, doi:10.1029/2006JD007695, 2006.

Pfister, G. G., Emmons, L. K., Hess, P. G., Lamarque, J.-F., Thompson, A. M., and Yorks, J. E.: Analysis of the summer 2004 ozone budget over the United States using Inter-

continental Transport Experiment Ozonesonde Network Study (IONS) observations and Model of Ozone and Related Tracers (MOZART-4) simulations, J. Geophys. Res., 113, D23306, doi:10.1029/2008JD010190, 2008.

Pfister, G. G., Parrish, D. D., Worden, H., Emmons, L. K., Edwards, D. P., Wiedinmyer, C., Diskin, G. S., Huey, G., Oltmans, S. J., Thouret, V., Weinheimer, A., and Wisthaler, A.: Characterizing summertime chemical boundary conditions for airmasses entering the US West Coast, Atmos. Chem. Phys., 11, 1769–1790, doi:10.5194/acp-11-1769-2011, 2011.

Pumphrey, H. C., Santee, M. L., Livesey, N. J., Schwartz, M. J., and Read, W. G.: Microwave Limb Sounder observations of biomass-burning products from the Australian bush fires of February 2009, Atmos. Chem. Phys., 11, 6285–6296, doi:10.5194/acp-11-6285-2011, 2011.

Randel W. J., Park, M., Emmons, L., Kinnison, D., Bernath, P., Walker, K. A., Boone, C., and Pumphrey, H.: Asian Monsoon Transport of Pollution to the Stratosphere, Science, 328, 611–613, 10.1126/science.1182274, 2010.

R'Honi, Y., Clarisse, L., Clerbaux, C., Hurtmans, D., Duflot, V., Turquety, S., Ngadi, Y., and Coheur, P.-F.: Exceptional emissions of NH_3 and HCOOH in the 2010 Russian wildfires, Atmos. Chem. Phys., 13, 4171–4181, doi:10.5194/acp-13-4171-2013, 2013.

Rinsland, C. P., Goldman, A., Murcray, F. J., Stephen, T. M., Pougatchev, N. S., Fishman, J., David, S. J., Blatherwick, R. D., Novelli, P. C., Jones, N. B., and Connor, B. J.: Infrared solar spectroscopic measurements of free tropospheric CO, C_2H_6, and HCN above Mauna Loa, Hawaii: Seasonal variations and evidence for enhanced emissions from the Southeast Asian tropical fires of 1997–1998, J. Geophys. Res., 104, 18667–18680, 1999.

Rinsland, C. P., Meier, A., Griffith, D. W. T., and Chiou, L. S.: Ground-based measurements of tropospheric CO, C_2H_6, and HCN from Australia at 34° S latitude during 1997–1998, J. Geophys. Res., 106, 20913–20924, 2001.

Rinsland C. P., Jones, N. B., Connor, B. J., Wood, S. W., Goldman, A., Stephen, T. M., Murcray, F. J., Chiou, L. S., Zander, R., and Mahieu, E.: Multiyear infrared solar spectroscopic measurements of HCN, CO, C_2H_6, and C_2H_2 tropospheric columns above Lauder, New Zealand (45° S latitude), J. Geophys. Res., 107, 4185, doi:10.1029/2001JD001150, 2002.

Rodgers, C. D.: Inverse methods for atmospheric sounding: Theory and Practice, Series on Atmospheric, Oceanic and Planetary Physics Vol. 2, World Scientific Publishing CO., Singapore, 2000.

Rodgers, C. D. and Connor, B. J.: Intercomparison of remote sounding instruments, J. Geophys. Res., 108, 4116–4129, 2003.

Sancho, P., De La Cruz, J., Diaz, A., Martin, F., Hernandez, E., Valero, F., and Albarran, B.: A five-year climatology of backtrajectories from the Izaña baseline station, Tenerife, Canary Islands, Atmos. Environ., 26, 1081–1096, 1992.

Sauvage, B., Thouret, V., Cammas, J.-P., Gheusi, F., Athier, G., and Nédélec, P.: Tropospheric ozone over Equatorial Africa: regional aspects from the MOZAIC data, Atmos. Chem. Phys., 5, 311–335, doi:10.5194/acp-5-311-2005, 2005.

Singh, H. B., Salas, L., Herlth, D., Kolyer, R., Czech, E., Viezee, W., Li, Q., Jacob, D. J., Blake, D., Sachse, G., Harward, C. N., Fuelberg, H., Kiley, C. M., Zhao, Y., and Kondo, Y.: In situ measurements of HCN and CH3CN over the Pacific Ocean: sources, sinks and budgets, J. Geophys. Res., 108, 8795, doi:10.1029/2002JD003006, 2003.

Standard Atmosphere: National Atmospheric and Oceanic Administration S/T 76–1562, US Government Printing Office, Washington DC, 1976.

Tilmes, S., Emmons, L. K., Law, K. S., Ancellet, G., Schlager, H., Paris, J.-D., Fuelberg, H. E., Streets, D. G., Wiedinmyer, C., Diskin, G. S., Kondo, Y., Holloway, J., Schwarz, J. P., Spackman, J. R., Campos, T., Nédélec, P., and Panchenko, M. V.: Source contributions to Northern Hemisphere CO and black carbon during spring and summer 2008 from POLARCAT and START08/preHIPPO observations and MOZART-4, Atmos. Chem. Phys. Discuss., 11, 5935–5983, doi:10.5194/acpd-11-5935-2011, 2011.

Van Damme, M., Clarisse, L., Heald, C. L., Hurtmans, D., Ngadi, Y., Clerbaux, C., Dolman, A. J., Erisman, J. W., and Coheur, P. F.: Global distributions, time series and error characterization of atmospheric ammonia (NH_3) from IASI satellite observations, Atmos. Chem. Phys., 14, 2905–2922, doi:10.5194/acp-14-2905-2014, 2014.

van der Werf, G. R., Randerson, J. T., Giglio, L., Collatz, G. J., Kasibhatla, P. S., and Arellano Jr., A. F.: Interannual variability in global biomass burning emissions from 1997 to 2004, Atmos. Chem. Phys., 6, 3423–3441, doi:10.5194/acp-6-3423-2006, 2006.

van der Werf, G. R., Randerson, J. T., Giglio, L., Collatz, G. J., Mu, M., Kasibhatla, P. S., Morton, D. C., DeFries, R. S., Jin, Y., and van Leeuwen, T. T.: Global fire emissions and the contribution of deforestation, savanna, forest, agricultural, and peat fires (1997–2009), Atmos. Chem. Phys., 10, 11707–11735, doi:10.5194/acp-10-11707-2010, 2010.

Viatte, C., Strong, K., Hannigan, J., Nussbaumer, E., Emmons, L. K., Conway, S., Paton-Walsh, C., Hartley, J., Benmergui, J., and Lin, J.: Identifying fire plumes in the Arctic with tropospheric FTIR measurements and transport models, Atmos. Chem. Phys., 15, 2227–2246, doi:10.5194/acp-15-2227-2015, 2015.

Vigouroux, C., Stavrakou, T., Whaley, C., Dils, B., Duflot, V., Hermans, C., Kumps, N., Metzger, J.-M., Scolas, F., Vanhaelewyn, G., Müller, J.-F., Jones, D. B. A., Li, Q., and De Mazière, M.: FTIR time-series of biomass burning products (HCN, C_2H_6, C_2H_2, CH_3OH, and HCOOH) at Reunion Island (21° S, 55° E) and comparisons with model data, Atmos. Chem. Phys., 12, 10367–10385, doi:10.5194/acp-12-10367-2012, 2012.

Volkamer, R., Ziemann, P. J., and Molina, M. J.: Secondary Organic Aerosol Formation from Acetylene (C_2H_2): seed effect on SOA yields due to organic photochemistry in the aerosol aqueous phase, Atmos. Chem. Phys., 9, 1907–1928, doi:10.5194/acp-9-1907-2009, 2009.

Walker, J. C., Dudhia, A., and Carboni, E.: An effective method for the detection of trace species demonstrated using the MetOp Infrared Atmospheric Sounding Interferometer, Atmos. Meas. Tech., 4, 1567–1580, doi:10.5194/amt-4-1567-2011, 2011.

Wespes, C., Emmons, L., Edwards, D. P., Hannigan, J., Hurtmans, D., Saunois, M., Coheur, P.-F., Clerbaux, C., Coffey, M. T., Batchelor, R. L., Lindenmaier, R., Strong, K., Weinheimer, A. J., Nowak, J. B., Ryerson, T. B., Crounse, J. D., and Wennberg, P. O.: Analysis of ozone and nitric acid in spring and summer Arctic pollution using aircraft, ground-based, satellite observations and MOZART-4 model: source attribution and partitioning, At-

mos. Chem. Phys., 12, 237–259, doi:10.5194/acp-12-237-2012, 2012.

Wiedinmyer, C., Quayle, B., Geron, C., Belote, A., McKenzie, D., Zhang, X., O'Neill, S., and Wynne, K.: Estimating emissions from fires in North America for air quality modeling, Atmos. Environ., 40, 3419–3432, 2006.

Wiedinmyer, C., Akagi, S. K., Yokelson, R. J., Emmons, L. K., Al-Saadi, J. A., Orlando, J. J., and Soja, A. J.: The Fire INventory from NCAR (FINN): a high resolution global model to estimate the emissions from open burning, Geosci. Model Dev., 4, 625-641, doi:10.5194/gmd-4-625-2011, 2011.

Wiegele, A., Glatthor, N., Höpfner, M., Grabowski, U., Kellmann, S., Linden, A., Stiller, G., and von Clarmann, T.: Global distributions of C2H6, C_2H_2, HCN, and PAN retrieved from MIPAS reduced spectral resolution measurements, Atmos. Meas. Tech., 5, 723–734, doi:10.5194/amt-5-723-2012, 2012.

Xiao, Y., Jacob, D. J., and Turquety, S.: Atmospheric acetylene and its relationship with CO as an indicator of air mass age, J. Geophys. Res.-Atmos., 112, D12305, doi:10.1029/2006JD008268, 2007.

Yienger, J. J., Galanter, M., Holloway, T. A., Phadnis, M. J., Guttikunda, S. K., Carmichael, G. R., Moxim, W. J., and Levy II, H.: The episodic nature of air pollution transport from Asia to North America, J. Geophys. Res., 105, 26931–26945, doi:10.1029/2000JD900309, 2000.

Yulianti N. and Hayasaka, H.: Recent Active Fires under El Niño Conditions in Kalimantan, Indonesia, American Journal of Plant Sciences, 4, 685–696, 2013.

Zander, R., Rinsland, C. P., Ehhalt, D. H., Rudolph, J., and Demoulin, P. H.: Vertical Column Abundances and Seasonal Cycle of Acetylene, C_2H_2, above the Jungfraujoch Station, Derived from IR Solar observations, J. Atmos. Chem., 13, 359–372, 1991.

Zhang, Q., Streets, D. G., Carmichael, G. R., He, K. B., Huo, H., Kannari, A., Klimont, Z., Park, I. S., Reddy, S., Fu, J. S., Chen, D., Duan, L., Lei, Y., Wang, L. T., and Yao, Z. L.: Asian emissions in 2006 for the NASA INTEX-B mission, Atmos. Chem. Phys., 9, 5131–5153, doi:10.5194/acp-9-5131-2009, 2009.

Zhao, Y., Strong, K., Kondo, Y., Koike, M., Matsumi, Y., Irie, H., Rinsland, C. P., Jones, N. B., Suzuki, K., Nakajima, H., Nakane, H., and Murata, I.: Spectroscopic measurements of tropospheric CO, C_2H_6, C_2H_2, and HCN in northern Japan, J. Geophys. Res., 107, 4343, doi:10.1029/2001JD000748, 2002.